

The Pennsylvania State University

The Graduate School

**CLASSIFICATION AND DISCRIMINATION OF DRONES
AND BIRDS USING MICRO-DOPPLER IMAGES**

A Thesis in

Electrical Engineering

by

Bryan Tsang

© 2022 Bryan Tsang

Submitted in Partial Fulfillment
of the Requirements
for the Degree of

Master of Science

August 2022

The thesis of Bryan Tsang was reviewed and approved by the following:

Ram Mohan Narayanan
Professor of Electrical Engineering
Thesis Advisor

Tim Kane
Professor of Electrical Engineering

Ramesh Bharadwaj
U.S. Naval Research Laboratory
Special Signatory

Kultegin Aydin
Professor of Electrical Engineering
Head of the Department

ABSTRACT

This master's thesis investigates the micro-Doppler characteristics of flying targets such as drones and birds for classification purposes. Through the implementation of a custom-designed 10-GHz radar system, measurements of different scenarios with a variety of targets are recorded to create a dataset for image classification. Using support vector machines (SVMs), classification results were achieved with high confidence for multiple problems. The impact of landscape and target behavior on micro-Doppler signatures is investigated. A 77-GHz FMCW is tested for measuring micro-Doppler characteristics of drones. The limitations regarding the experimental process are explained thoroughly, with suggestions on future avenues regarding this work.

TABLE OF CONTENTS

LIST OF FIGURES	vi
LIST OF TABLES	x
ACKNOWLEDGEMENTS	xi
Chapter 1 – Introduction	1
1.1 - Motivation.....	1
1.2 – Problem Statement	2
1.3 – Contributions.....	3
1.4 – Thesis Limitations.....	4
1.5 – Thesis Overview	4
Chapter 2 – Concepts and Theory.....	5
2.1 – Radar Basics.....	5
2.2 – Continuous Wave Micro-Doppler.....	5
2.3 – FMCW Radar.....	9
Chapter 3 – Radar Systems	15
3.1 – 10-GHz Radar System.....	15
3.1.1 – Block Diagram	19
3.2 – 77-GHz Radar System.....	20
3.2.1 mmWave Studio.....	24
3.3 Radar System Limitations	30
3.3.1 10-GHz Radar Limitations	30
3.3.2 77-GHz Radar Limitations	32
Chapter 4 – Experimental Results.....	34
4.1 – Simulation Setup	34
4.2 – Data Collection Process	40
4.3 – UAVs	46
4.3.1 – UAV Detection Scenarios	48
4.4 – Birds	53
4.5 – FMCW Micro-Doppler mmWave Studio Results.....	58
4.6 Experimental Limitations.....	61
Chapter 5 – Classification.....	63
5.1 – Spectrogram Generation.....	63
5.2 – Support Vector Machine	66
5.3 – Drone Classification.....	67
5.4 – Binary Classification.....	71

5.5 – 5-Class Classification.....	72
5.6 – Classification Limitations	73
Chapter 6 – Conclusions	74
References.....	75

LIST OF FIGURES

Figure 1: Radar interaction with a single quadcopter rotor.....	6
Figure 2: Power spectral density (left) and spectrogram (right) of a single propeller.	7
Figure 3: Frequency modulation visualization.....	9
Figure 4: FMCW tradeoff for different target information.....	10
Figure 5: Corner reflector mmWave Studio experiment.....	11
Figure 6: Corner reflector range FFT plot.	12
Figure 7: Range vs time corner reflector plot.	12
Figure 8: Range-Doppler response of the corner reflector.....	13
Figure 9: Corner reflector spectrogram.....	14
Figure 10: The 10-GHz radar system setup.	16
Figure 11: 30° LOS antenna setup.	17
Figure 12: RF front-end.	17
Figure 13: CW RF front-end block diagram.....	19
Figure 14: The 77-GHz device: Texas Instruments DCA1000EVM + AWR1642BOOST. ...	20
Figure 15: Antenna gain vs. theta. ⁹	22
Figure 16: Range radar demo with the mmWave Software Development Kit.	23
Figure 17: mmWave Studio connection setup.	24
Figure 18: mmWave Studio static configuration window.	25
Figure 19: mmWave Studio data configuration window.	26
Figure 20: mmWave Studio sensor configuration window.....	26
Figure 21: mmWave Studio post-processing.	28
Figure 22: Corner reflector range-velocity map comparison.	29
Figure 23: mmWave Studio constant stream tab.	29

Figure 24: I/Q time signal plots.	31
Figure 25: FFT power spectral densities before and after I/Q correction.	31
Figure 26: Spectrograms before and after I/Q correction.	32
Figure 27: Simulated quadcopter time signal.	36
Figure 28: Simulated quadcopter frequency response.	36
Figure 29: Simulation quadcopter spectrogram.	37
Figure 30: Spectrograms with different window sizes.	38
Figure 31: Simulated quadcopter results (shortened integration time).	39
Figure 32: Different rotation accelerations.	39
Figure 33: Initial indoor quadcopter micro-Doppler detection test.	40
Figure 34: Stationary drone data collection setup.	41
Figure 35: Outdoor drone data collection setup.	41
Figure 36: Akaso UAV with reflective tape on the blade tip.	42
Figure 37: 0° LOS reflective tape on a rotor.	42
Figure 38: 30° LOS reflective tape on a rotor.	43
Figure 39: Recorded raw data in Audacity.	43
Figure 40: Chaptfor ground truth.	44
Figure 41: Generated Spectrogram in MATLAB based on raw data.	45
Figure 42: PSI Studio FFT feature.	45
Figure 43: Metabird (small) and its associated spectrogram.	47
Figure 44: Akaso drone (medium) and its associated spectrogram.	47
Figure 45: BlackHawk drone (big) and its associated spectrogram.	48
Figure 46: Outdoor against-the-wall setup.	49
Figure 47: Wall vs. free space spectrogram comparison.	50
Figure 48: Around-the-corner UAV detection.	50

Figure 49: Around-the-corner vs. free space spectrograms.	51
Figure 50: Tree foliage UAV detection.	51
Figure 51: Tree foliage spectrogram.	52
Figure 52: Metabird and real bird in the same recording.	52
Figure 53: Stationary vs. rotating antenna UAV detection.	53
Figure 54: Bird data collection setup.	54
Figure 55: Bald eagle and its associated spectrogram.	55
Figure 56: Golden eagle and its associated spectrogram.	55
Figure 57: Broad-winged hawk and its associated spectrogram.	56
Figure 58: American kestrel and its associated spectrogram.	57
Figure 59: Bald eagle spectrograms flying lower vs. flying higher.	57
Figure 60: FMCW micro-Doppler within mmWave Studio.	59
Figure 61: Outdoor UAV flight spectrogram.	59
Figure 62: UAV micro-Doppler at 2 meters away.	60
Figure 63: Range-speed response of an indoor UAV flight.	60
Figure 64: Metabird micro-Doppler through mmWave Studio.	61
Figure 65: Early data sorting inefficiencies.	64
Figure 66: Expedited Audacity recording segment snipping.	65
Figure 67: UAV spectrograms with removed axes and labels.	65
Figure 68: Bird spectrograms with removed axes and labels.	66
Figure 69: Confusion matrix results of classifier comparison for drone distinguishing.	67
Figure 70: UAV rotor acceleration spectrograms.	68
Figure 71: Deceptive spectrogram shows a UAV rising but coming to a hover with a falling shape.	68
Figure 72: Spectrogram shows a UAV falling and coming to a hover but with a rising shape.	69

Figure 73: Drone motion state model summary.....	70
Figure 74: Drone motion state classification accuracy and loss.	70
Figure 75: Drones vs. birds confusion matrix.....	71
Figure 76: 5-Class confusion matrix.....	72

LIST OF TABLES

Table 1: Sensing methods advantages and disadvantages.	2
Table 2: RF component list.....	18
Table 3: Radar parameters.	20
Table 4: SDR radar parameters.....	27
Table 5: Simulation parameters.	34
Table 6: UAV characteristics.....	46
Table 7: Bird characteristics.	54

ACKNOWLEDGEMENTS

I would like to thank my advisor Professor Ram Narayanan for his guidance, patience, and support throughout this master student's journey. I would also like to thank Dr. Ramesh Bharadwaj of the US Naval Research Laboratory (NRL) for his suggestions and for taking the time to serve on my thesis committee. A massive shoutout to my lab mates: Fred Chache, Terell Dale, Mark Pawelski, Ricky Washington, and Nick Munson for keeping me sane over the past two years. I would also like to thank Marc Navagato, Tyler Ridder, and Logan Hall for their aid and input regarding the design and development of practical radar systems. Thanks also go to Professor Tim Kane for serving on my thesis committee and providing insights.

A big thank you to the team at Shaver's Creek for assisting in the collection of bird flight recordings: Abigail Flanders, Joseph Whitehead, Shannon Davidow, Jon Kauffman, Jack Meyer, and Joshua Potter. Lastly, I would like to thank my parents for their unwavering kindness and support throughout my life.

This work was supported by the US Office of Naval Research Grant Number N00014-20-1-2064. The findings and conclusions presented in this thesis do not necessarily reflect the view of the funding agency.

Chapter 1 – Introduction

1.1 - Motivation

With the advent of commercial UAVs (Unmanned Aerial Vehicles), drone detection is becoming more of a necessity in recent years. The remote operative capabilities of UAVs pose a threat to security, privacy, and other potential legality issues. Additionally, the number of applications for UAV usage has also increased, ranging from recreational, commercial, and militaristic uses. Most modern drones are equipped with video cameras and can even deliver small packages. State-of-the-art drone usage now even contains methods for supplying wireless aid in forms of networking capabilities and more.

The cheap costs of UAVs paired with remote operability allow anyone to become a pilot. Many hazards may be overlooked if used incorrectly, resulting in an increased degree of risk.

Fortunately, the Federal Aviation Administration (FAA) created the Part 107 regulations for commercial small UAVs in June 2016. These regulations require UAV pilots to register their UAVs if they weigh between 0.55 – 55 lbs. In addition, the pilot must carry a small UAV operator license which can be obtained after passing the Part 107 exam. This exam covers a wide range of information regarding UAV safety. Some topics include UAV limitations, flight operations, airspace classification and operating requirements, flight restrictions, weather awareness, emergency procedures, radio communication procedures, and more.

Although these guidelines were created to improve awareness and overall UAV safety, the ease of accessibility to these systems can prove to be dangerous. People with malicious intentions pay no heed to the warnings and rules created by the FAA. For example, in 2018,

hundreds of flights were canceled at Gatwick Airport due to a drone sighting close to the runway, causing flight delays for 2 days.¹

1.2 – Problem Statement

State-of-the-art techniques for detecting drones include acoustic, optical, and radar methods. Despite these wide ranges of sensing practices, there are several tradeoffs associated with each method. In Table 1, the advantages and disadvantages are listed sensing drones with acoustics, cameras, lidar, and radar.

Table 1: Sensing methods advantages and disadvantages.

	Advantages	Disadvantages
Acoustics	<ul style="list-style-type: none"> - No LOS - Low visibility - Low cost 	<ul style="list-style-type: none"> - Ineffective in noisy conditions - Wind conditions
Cameras	<ul style="list-style-type: none"> - Easiest operability - High Accuracy 	<ul style="list-style-type: none"> - Very sensitive operability - High cost
Lidar	<ul style="list-style-type: none"> - High Accuracy 	<ul style="list-style-type: none"> - Expensive - Weather dependent - Small FOV
Radar	<ul style="list-style-type: none"> - Low-cost - Weather resistant - Robust 	<ul style="list-style-type: none"> - Targets have small RCS

Some of the advantages of acoustics include no Line-Of-Sight (LOS) requirements, effective performance in low-visibility conditions, and a relatively low cost for implementation. But, in noisy conditions like windy gusts, the microphones will not be able to distinguish or detect the drone. Using cameras for detecting targets is advantageous due to the high accuracy and easy operability. Although it's easy to detect flying targets, it becomes difficult to further classify the subject. There is also a high cost associated with using and maintaining cameras. Lidar is an accurate method for detecting targets, but the cons greatly outweigh the pros. They are

expensive, have a narrow LOS, and are heavily weather dependent. Lastly, radar provides an effective method for detection due to the low cost of implementation and robustness of operability. The biggest weakness of using radar is that targets tend to have low Radar Cross Sections (RCS) which can hinder the ability to detect a target.

RCS-based radar methods such as high-resolution range profiles and Synthetic Aperture Radar (SAR) can be difficult when considering the similar RCS values of birds and drones.²⁻⁵ To avoid this, the benefits of leveraging the micro-Doppler signatures from targets are investigated using a Continuous Wave (CW) radar system and a Frequency Modulated Continuous Wave (FMCW) Software Defined Radio (SDR) system. Through processing algorithms, it is possible to discern the type of target (bird or drone) based on their micro-motions such as propeller blades spinning or bird wing flapping.

For Automatic Target Recognition (ATR) purposes, many current studies utilize machine learning to classify images of micro-Doppler signatures between drones and birds. Unfortunately, a lack of real-world data makes improving classification efforts difficult.

1.3 – Contributions

Within this thesis, contributions revolve around the study of micro-Doppler signatures present in consumer UAVs with the addition of birds from Shaver's Creek, a local bird sanctuary. A dataset is created using a 10-GHz radar system optimized and built in-house, containing over 750 images of drones and birds. Also, tests were conducted to observe the influence of various detection scenarios when visualizing UAV micro-Doppler. In addition, initial tests were conducted with an FMCW for optimizing the detectability of UAVs with a commercial 77-GHz SDR. Lastly, classification efforts are made for distinguishing different problems like drones vs. birds and characterizing different UAV vertical motion states.

1.4 – Thesis Limitations

Some limitations arose due to the time constraints within this operation. Hardware constraints played a large role in deterring the clarity within some micro-Doppler images. Designing and setting up the radar systems required a significant amount of troubleshooting and maintenance. Signal processing and classification methods could have been explored deeper, but the results obtained are satisfactory for this work. Lastly, obtaining copious amounts of data was difficult due to weather and bird behavior.

1.5 – Thesis Overview

The overview of this thesis is as follows: Chapter 2 discusses the concepts and theory regarding radar and drone detection. Chapter 3 dives into the design and operability of the radar systems. Chapter 4 outlines the experimental setup and results obtained. Within Chapter 5, classification setup and tactics are described. In Chapter 6, a conclusion of the thesis is provided with possible directions for future research.

Chapter 2 – Concepts and Theory

Within this chapter, concepts regarding radar fundamentals and signal processing techniques will be dissected.

2.1 – Radar Basics

Radar (**radio detection and ranging**) is used by transmitting radio waves at frequencies between 300 MHz and 300 GHz. In a CW device, these signals are transmitted at a single frequency from the radar system and targets within the Field Of View (FOV) are illuminated and refract the signals in distinct directions. Reflected signals that return to the radar system are collected by the receive antenna. Movement from targets results in a difference in frequency between the transmitted signal and the received signal, which is known as the Doppler frequency. This frequency shift denotes the velocity at which the target is radially moving to the radar.

2.2 – Continuous Wave Micro-Doppler

As mentioned previously, radar has been proven to be a sound method for classifying targets through leveraging micro-Doppler. Micro-Doppler is the presence of micro rotations, vibrations, or periodic motions that can be observed when extracting Doppler information from a target. For a drone, these periodic vibrations occur from blades spinning through the rotor which generates thrust and propels the UAV into the air. Quadcopters can maneuver with remote control through the manipulation of rates of rotation and the amount of thrust produced within each rotor.

A study goes into depth on the equations used for discerning micro-Doppler signatures from drones.⁶ The equation for Doppler frequency is given by

$$f_d = 2v_r/\lambda \quad (1)$$

where v_r is the radial velocity of the target and λ is the wavelength. The corresponding λ for a 10-GHz carrier frequency is 3 cm. A rotor's rotational velocity, ω , in revolutions per second is related to the maximum v_r expected of the blade tip through

$$\omega = v_r/2\pi l \quad (2)$$

where l is the blade length. In the simulations to follow, ω is modeled at 56 revolutions per second, which corresponds to a v_r value of 35.2 m/s for an l value of 10 cm. This maps to an expected maximum Doppler shift around 2.35 kHz occurring at the blade tips. It is assumed that the blade is along the LOS of the radar. Most UAVs have two or three blades associated with each rotor. Figure 1 shows how the radial component of the rotating blade changes over time.

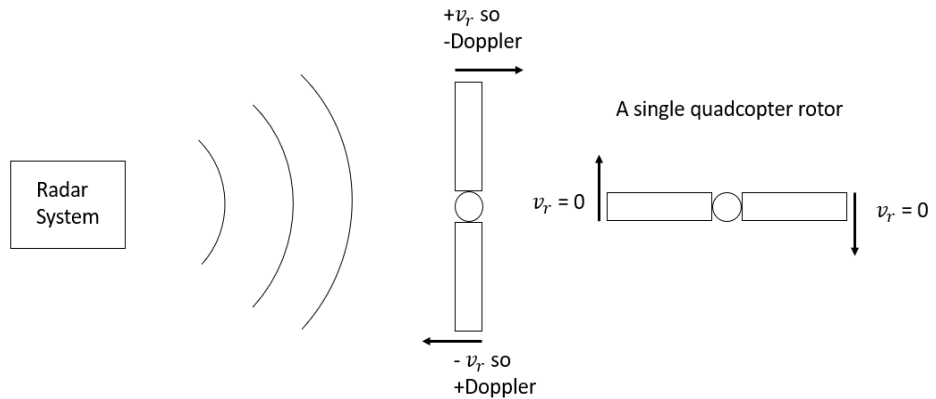


Figure 1: Radar interaction with a single quadcopter rotor.

The radar system transmits a continuous signal at a single frequency. These signals bounce off the rotating propellers and radar receives these reflected signals. The radial velocity, v_r , of the spinning blade tips, does not remain constant, but the periodicity can be modeled with the use of a velocity-time plot, a spectrogram. In addition, a simple Fast Fourier Transform (FFT) of the raw data provides a power spectral density plot that denotes peaks at frequencies, corresponding to the radial velocities observed within the recording. An FFT takes a window size of samples and computes the power spectral density of that instance. The spectrogram is known as the Short-Time Fourier Transform (STFT) which computes multiple FFTs and displays them as frequency or velocity over time. In Figure 2, the power spectral density and the spectrogram of a single propeller are shown.

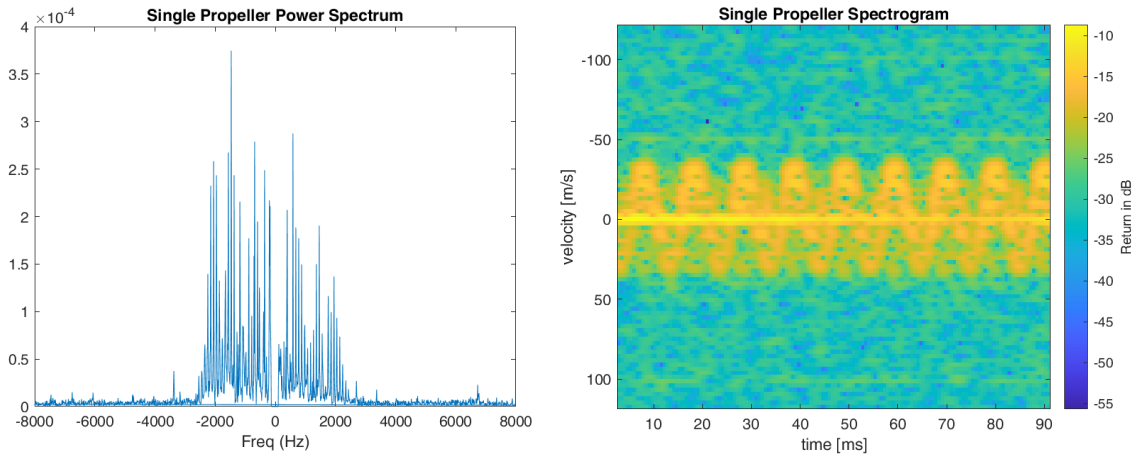


Figure 2: Power spectral density (left) and spectrogram (right) of a single propeller.

As the blade moves horizontally along the radar's LOS, v_r becomes 0. When the blade begins to move directly to or away from the radar, the maximum v_r values are detected. A target moving towards the radar refers to a positive (+) Doppler shift while a target moving away results in a negative (-) Doppler shift. The maximum peaks in the power spectrum are around 2.5 kHz.

In the resulting spectrogram, the maximum velocity is confirmed to be roughly 37.5 m/s which is per equation 1.

Additional Doppler frequencies can be caused due to the main body movement of the drone. For a moving drone, the maximum Doppler shift is given by:

$$f_d = f_{d_body} + f_{d_micro-Doppler} \quad (3)$$

where f_{d_body} is the Doppler shift induced by the main body movement of the drone. Since the radar system measures radial velocity, the look angle from the radar to the target plays a vital role in the displayed Doppler frequency. Equation 3 can be rewritten when considering angle dependence:

$$f_d = (f_{d_{body}} + f_{d_{micro-Doppler}}) * \cos(\theta) \quad (4)$$

where θ is the incident angle from the radar to the target.

Micro-Doppler of flying objects will vary from target to target. For instance, a quadcopter signature will be different than a fixed plane or a helicopter. In addition, many surveillance systems confuse drones with birds due to their similar sizes and speeds. Conveniently, the micro-Doppler phenomenon is a great discriminator of the two classes. In birds, the micro-Doppler of the flapping pattern produces a periodic shape but is not as strong and quick as a drone. The RPM for a drone can exceed 6000 RPM but the wing flaps of a bird are much slower. Through the implementation of spectrograms, micro-Doppler signatures of different flying targets can be classified.

The mechanics of a drone in flight are unique. By generating thrust through the rotation of 4 motors, each with 2 blades attached, UAVs can support their weight and ascend. Different combinations of rotation speed will result in different UAV flight motions. In this study, the weight and size of the target will be discriminating factors for which micro-Doppler signature belongs to which target. For heavier UAVs, more thrust is required to lift the drone, resulting in a higher detected micro-Doppler bandwidth.

2.3 – FMCW Radar

Range information can be extracted by modulating these radio signals either through frequency or amplitude. In a Frequency Modulated Continuous Wave (FMCW) radar, the frequency is shifted linearly in a periodic fashion. The periodic shape in Figure 3 is known as a sawtooth chirp. As time progresses, the frequency increases. After reaching the max frequency, it drops down to the lowest frequency and repeats the cycle.

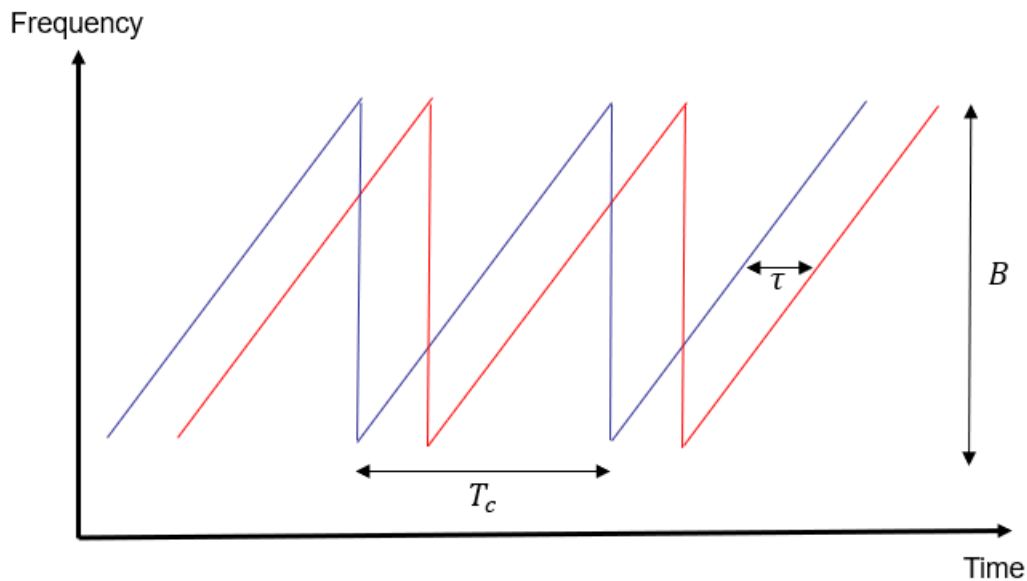


Figure 3: Frequency modulation visualization.

In blue is the transmitted signal and in red is the received signal. To obtain the range of the target, the time difference is measured between the transmitted and received signal. At an arbitrary time, t , the time delay between the transmitted and received signal's corresponding frequency gives information on the location of the target through the fast time Fourier Transform. Velocity information can be obtained by using a 2D FFT. Among different ranges, the FFT is taken over what is known as the short time to create a Velocity vs. Time plot.

Unlike CW radar systems, the method for extracting Doppler information is more complex since performing the FFT on a frequency modulated signal yields range information. In Figure 4, a graphic is provided by Texas Instruments regarding mapping requirements to chirp parameters.⁷

Mapping requirements to Chirp Parameters

Given range resolution (d_{res}), max range (d_{max}), velocity resolution (v_{res}), max velocity (v_{max}), how do we design a frame?. Lets sketch a possible design method

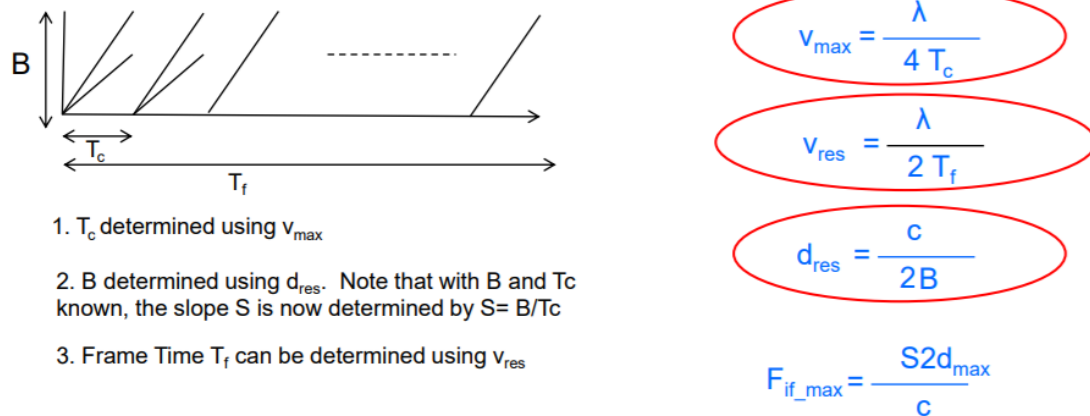


Figure 4: FMCW tradeoff for different target information.

The maximum unambiguous velocity is governed by the wavelength and the length of each chirp. By reducing the chirp length, a higher detectable velocity is possible. The velocity

resolution is dictated by the total frame time. The longer the frame, the finer the velocity resolution. Range resolution is dependent on the bandwidth of the frequency modulation. With higher bandwidth, the range resolution becomes finer. Lastly, the maximum range can be found by understanding the relationship between the slope of the frequency modulation and the maximum possible sampling rate.



Figure 5: Corner reflector mmWave Studio experiment.

To test out mmWave Studio, a simple experiment was conducted. Figure 5 shows a corner reflector moving toward the radar over a few seconds. The .bin file produced through mmWave Studio is read within the MATLAB environment and several graphs are constructed to assess the competence of mmWave Studio's post-processing. The first is a range FFT plot, shown in Figure 6.

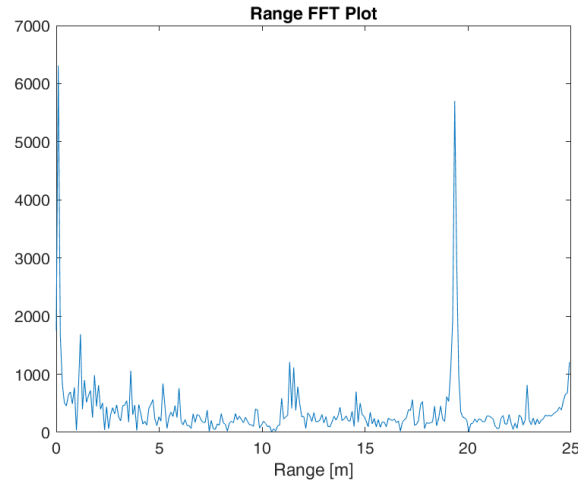


Figure 6: Corner reflector range FFT plot.

Within this FFT plot, the magnitude is shown on the left axis and the range is shown on the bottom. The corner reflector has a significantly higher RCS than everything else in the radar's FOV, so the large peak around 19 meters corresponds to the target. There are some smaller peaks present around 11 meters which are due to the vehicles on the side.

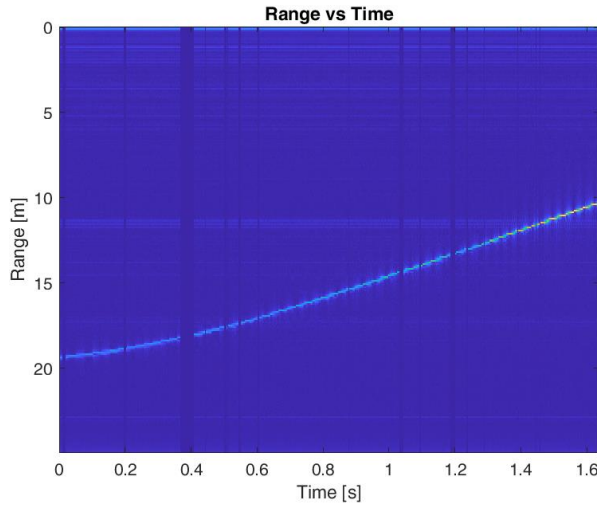


Figure 7: Range vs time corner reflector plot.

Figure 7 displays a range vs time plot. Throughout the duration, the range is accurately depicted with the corner reflector coming closer to the radar system. As the corner reflector moves closer to the radar, the signal strength also increases. For the stationary vehicles around 11 meters, a faint, horizontal line can be seen. Next, Figure 8 shows a range-Doppler response, generated to display the range and velocity of the observed targets at a given frame.

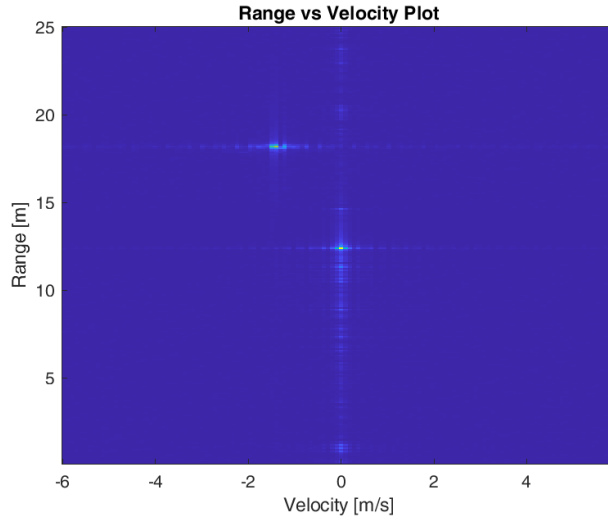


Figure 8: Range-Doppler response of the corner reflector.

The range-Doppler response displays two distinct targets. The corner reflector is moving toward the radar so a velocity of around -1.7 m/s is observed. Since this response is generated with samples at the start of the recording, a range around 18 meters is noted. The stationary vehicles are shown at a range of around 13 meters, with a velocity of 0 m/s.

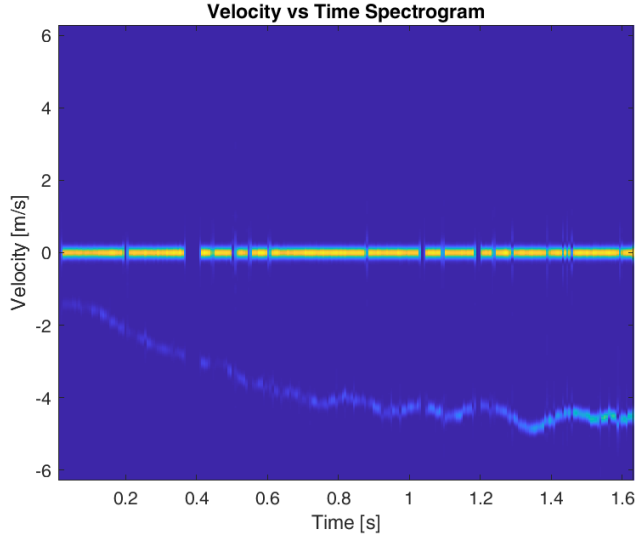


Figure 9: Corner reflector spectrogram.

Next, a spectrogram is generated by converting the .bin file into a velocity vs time plot. As shown in Figure 9, it can be seen as the corner reflector increases velocity over time and steadies out around -4.4 m/s. In both Figures 7 and 9, samples are missing with the most noticeable around the 0.4-second mark. This is due to dropped packets, acknowledged within the mmWave Studio user manuals.

Chapter 3 – Radar Systems

Within this thesis, two radar systems are used for experimentation. First, a 10-GHz CW radar is designed for collecting and creating a dataset for micro-Doppler signatures. Second, a 77-GHz FMCW software-defined radar is used to investigate the capabilities of using a mmWave device for drone detection.

3.1 – 10-GHz Radar System

To begin, a 10-GHz frequency was chosen due to its optimality between low and high frequencies. If the frequency of the signal is too low, the Doppler information will not be sufficient for the accurate realization of the target's micro-Doppler signature. On the other hand, if the frequency is too high, the cost of the radar system becomes more expensive and the phase requirements for components become too stringent.

The radar system went through multiple different designs, and the final product is shown in Figure 10.

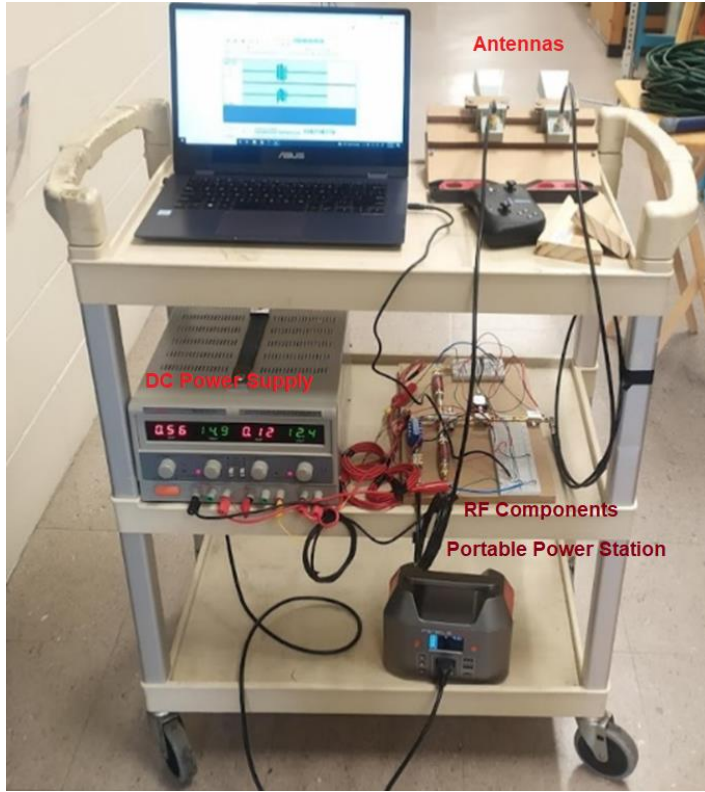


Figure 10: The 10-GHz radar system setup.

The 10-GHz radar system setup consists of three shelves. The top shelf contains the laptop and the horn antennas. The middle shelf is home to the DC power supply and the RF components of the 10-GHz system. The bottom shelf carries the portable power station which supports the DC Power Supply.

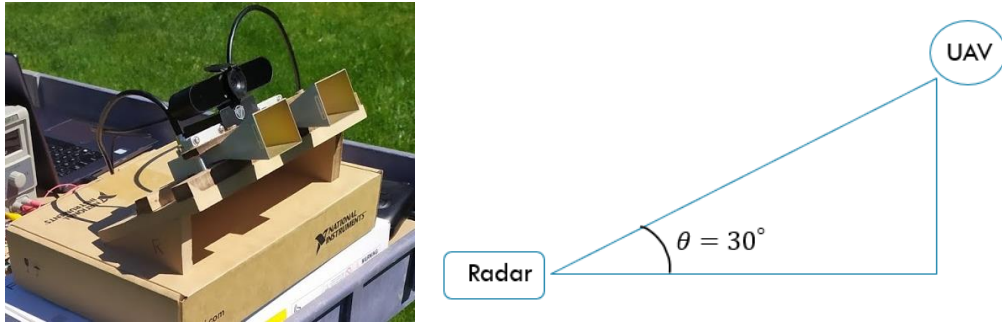


Figure 11: 30° LOS antenna setup.

The horn antennas are configured on a wooden mount, pointed at 30° above the horizon, as shown in Figure 11. There is also a webcam placed above the horn antennas for ground truth when recording data. By using a 30° look angle, the micro-Doppler signatures of the drones are more pronounced which will be discussed in greater depth in Chapter 4. The antennas are set up in a HH polarization state, which has been shown to provide the best UAV detection results.⁸

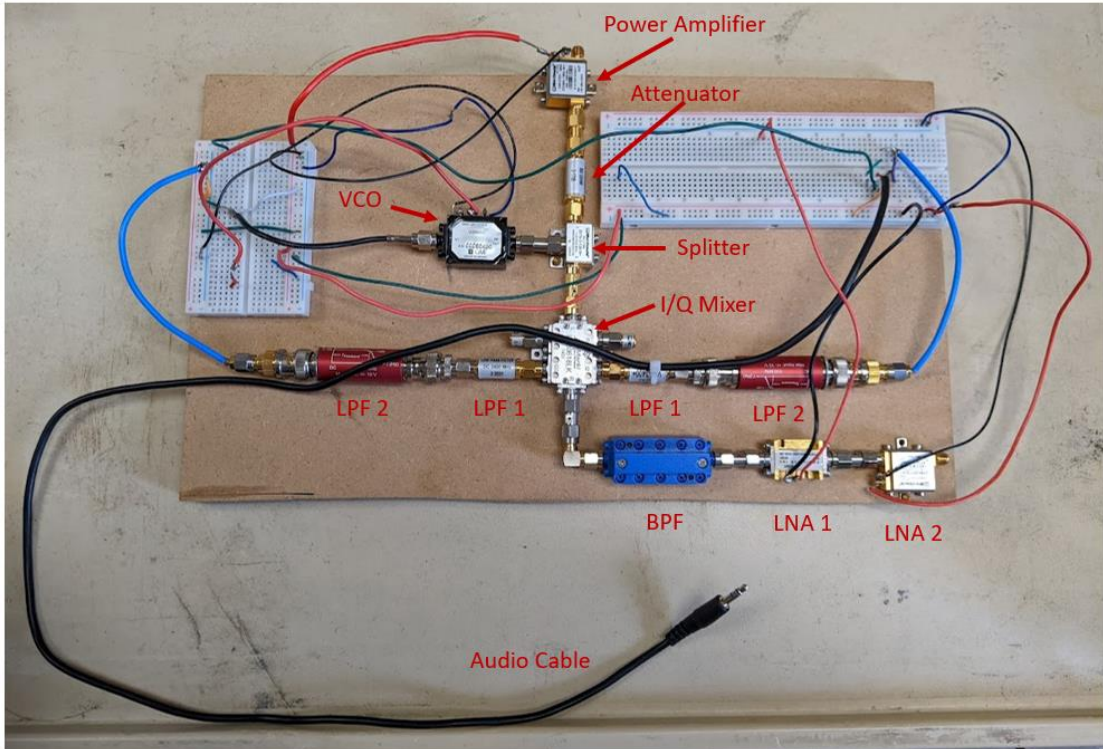


Figure 12: RF front-end.

The RF front-end is pictured in Figure 12. These components were purchased online through Mini-circuits, Thorlabs, and eBay. A component list is attached in Table 2.

Table 2: RF component list.

RF Component	Part #	Operating Frequency	Gain	Noise Figure	Output	VDC	Current	Supplier
VCO	V2555C	9.95 – 10.66 GHz	–	–	+12 dBm	12 V	150 mA	GMI
Power Splitter	ZX10-2-126-S+	7.4 – 12.6 GHz	–	–	–	–	–	Mini-Circuits
Attenuator	FW-12+	DC – 12 GHz	–	–	–	–	–	Mini-Circuits
Power Amplifier	ZX60-183-S+	6 – 18 GHz	23dB	–	+18.5dBm	5 V	260 mA	Mini-Circuits
Horn Antenna	WR90	8.2 – 12.4 GHz	10 dBi	–	–	–	–	A-infoMW
Low-Noise Amplifier 1	APTMP 5-080012 00-3025-D6	8 – 12 GHz	40 dB	3 dB	+25 dBm	15 V	450 mA	AmpliTech
Low-Noise Amplifier 2	ZX60-05113LN+	5 – 11 GHz	19 dB	1.8 dB	+12.2dBm	5 V	42 mA	Mini-Circuits
Band Pass Filter	ZVBP-10R5G-S+	DC – 40 GHz	–	–	–	–	–	Mini-Circuits
Frequency Mixer	IQB061 8LK	6 – 18 GHz	–	–	–	–	–	Marki Microwave
Low Pass Filter 1	VLF-3400+	DC – 3.4 GHz	–	–	–	–	–	Mini-Circuits
Low Pass Filter 2	EF502	DC – 100 kHz	–	–	–	–	–	Thorlabs

3.1.1 – Block Diagram

The block diagram associated with the RF front-end in Figure 12 is shown in Figure 13.

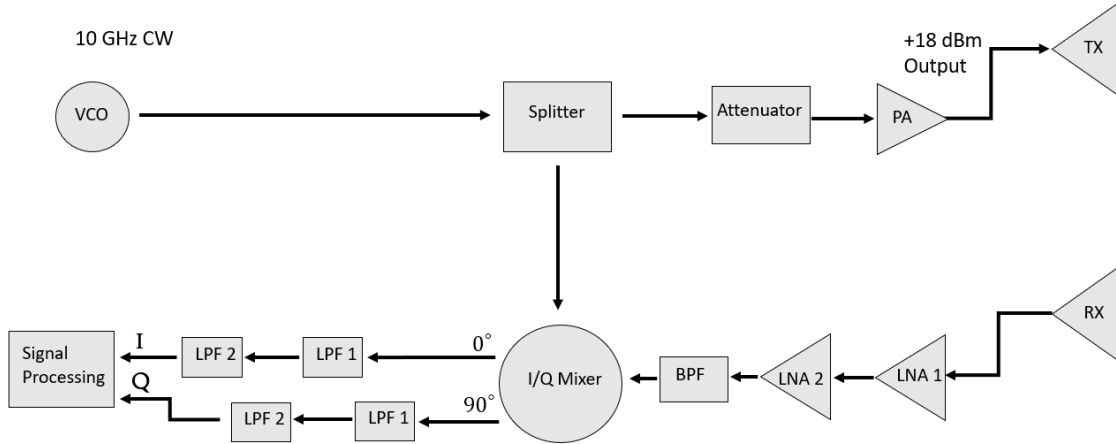


Figure 13: CW RF front-end block diagram.

The 10-GHz signal is generated by powering the Voltage-Controlled Oscillator (VCO) with a 12-V power supply. This signal is sent to the splitter where half of the power is sent to the transmit chain and the rest is sent to the I/Q mixer. This step is necessary to compare and mix the transmit and receive signals to obtain the Doppler frequencies. To avoid saturation within the power amplifier, a 12 dB attenuator is used to reduce the output power before amplification. A +18 dBm power output is transmitted through a 10 dB gain horn antenna.

After the signal reflects off a target, the signal is received through an identical horn antenna and fed through two low-noise amplifiers. Next, the signal goes through a bandpass filter to filter any undesired reflections or clutter. This filtered signal is mixed with the local oscillator signal to produce the Doppler frequency in two channels. The in-phase channel maintains the pure Doppler signal while the quadrature channel implements a 90° phase shift. Both signals are passed through

two low pass filters before going through an auxiliary cable to be processed within a laptop environment through MATLAB. The parameters of the radar system are given in Table 3.

Table 3: Radar parameters.

Parameter	Value
Frequency	10 GHz
Waveform	CW
Transmit Power	+18 dBm
Antenna Gain	10 dBi
Sampling Rate	12 ksps
Sampling Interval	0.5 seconds

3.2 – 77-GHz Radar System

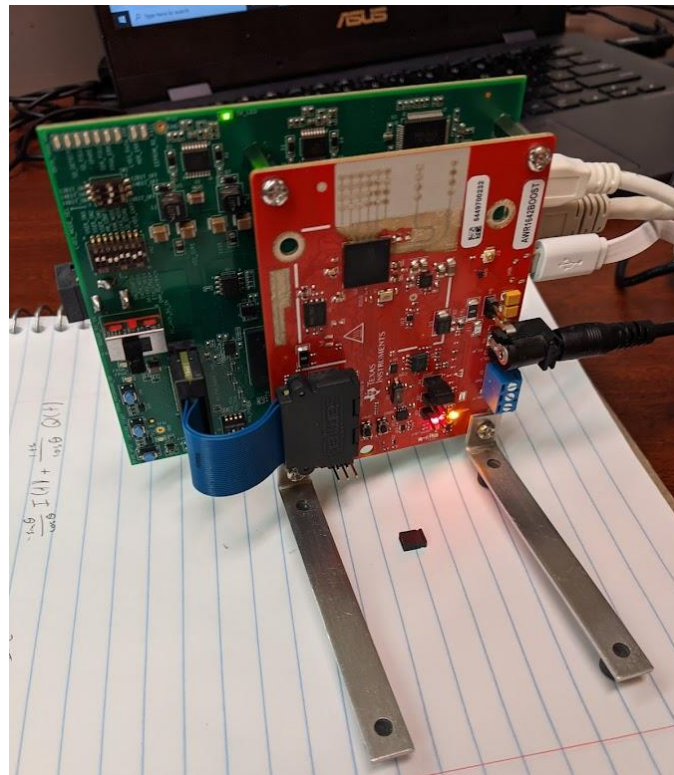


Figure 14: The 77-GHz device: Texas Instruments DCA1000EVM + AWR1642BOOST.

Figure 14 depicts the setup for the 77-GHz radar. This system is a Software Defined Radio (SDR) designed by Texas Instruments. It is a mmWave automotive radar experience kit that consists of two components, the DCA1000EVM (green) and the AWR1642BOOST (red). The AWR1642BOOST evaluation module is supported by the mmWave Software Development Kit (SDK) and mmWave Studio. This device contains an onboard antenna, micro-USB controller, 5V power jack, an XDS110 emulator, a CAN-FD Connector, SOP controls, and a 60pin HD connector. The AWR1642BOOST is powered through a 5V power jack, supplied by the portable power station. The connection to the PC is established by using a micro-USB cable to connect to the onboard XDS110 emulator. After connecting and powering the device, the PC device manager will recognize the XDS110 in the COM ports.

The onboard antennas contain four receivers and two transmitters that allow multi-object tracking along with distance and angle estimation. The peak antenna gain is 10 dBi over a frequency range of 76 to 81 GHz. A simulated gain plot for the angle at 78.5 GHz is shown in Figure 15.⁹

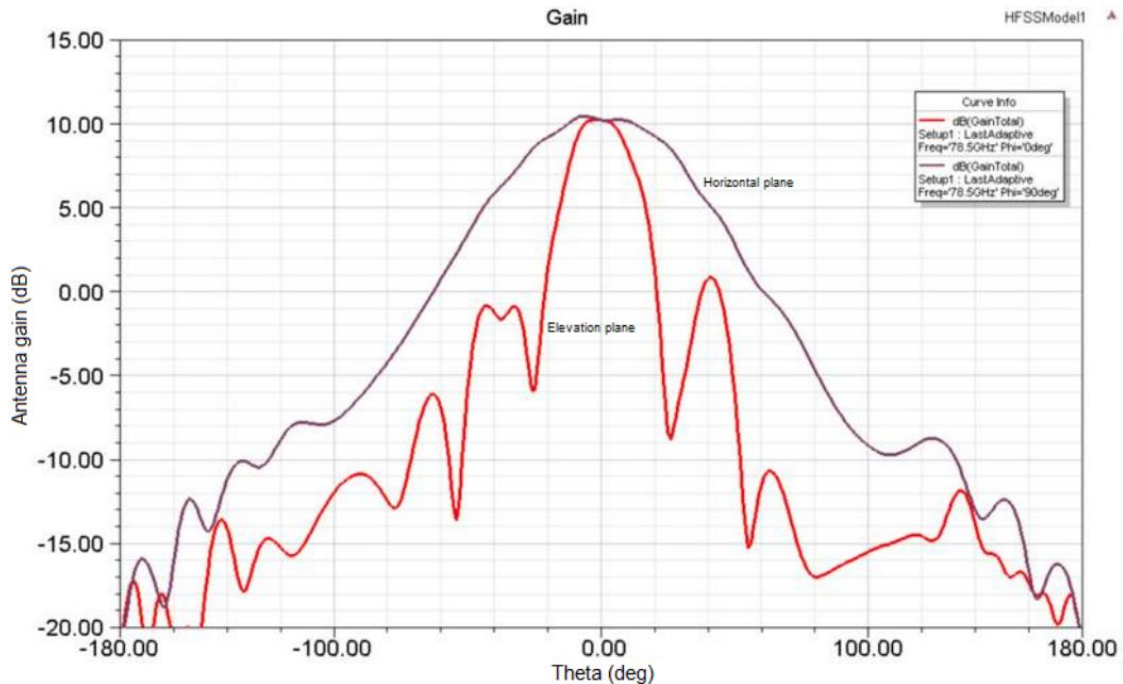


Figure 15: Antenna gain vs. theta.⁹

The mmWave SDK contains a series of evaluation applications. The automotive toolbox within the SDK provides in-depth tutorials and explanations of experiments. A few applications include in-cabin heartbeat sensing, automated parking demo, obstacle detection, and beam steering.

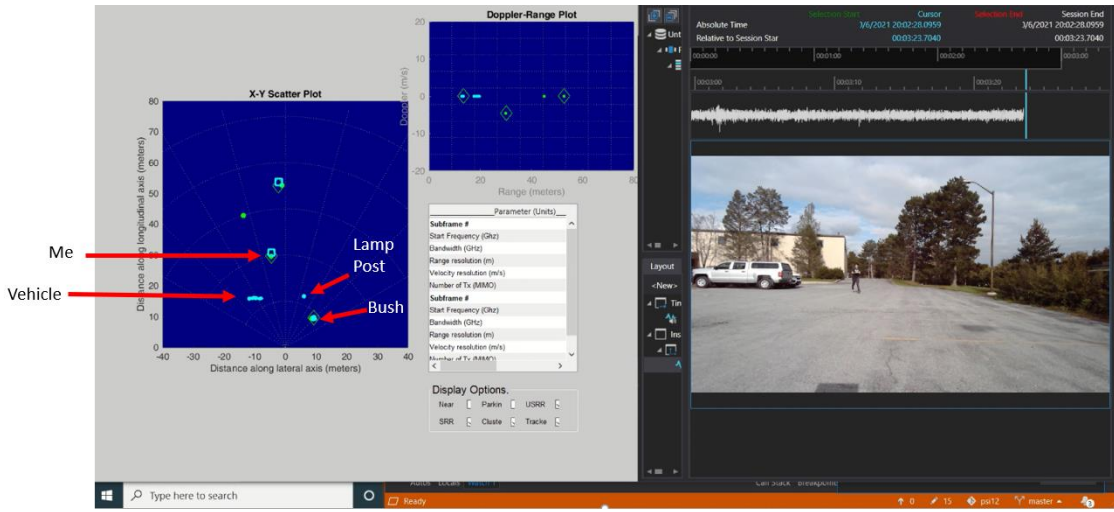


Figure 16: Range radar demo with the mmWave Software Development Kit.

In Figure 16, a demonstration is shown of utilizing PSI Studio with a demo within the mmWave SDK. For this test, the AWR1642BOOST is programmed to operate as a short-range radar that can detect objects up to 80 meters away. In the experiment setup, the target is running with a corner reflector toward the radar. In the X-Y scatter plot, targets detected by the SDR are displayed for downrange and lateral range. In the Doppler-Range plot, the velocity of each target is shown as well as their radial distance. In PSI Studio, the ground truth is verified through the video stream.

The caveat regarding the mmWave SDK is that the parameters for the experiment cannot be changed. The radar settings and the visualization screen are predetermined without any way for the user to customize each experiment. For this reason, the DCA1000EVM and mmWave Studio are used for drone and bird observations. With the addition of these tools, the users can build their experimental situations.

The DCA1000EVM is a data capture card that supports interfacing with the AWR1642BOOST which allows users to stream ADC data through ethernet. The DCA1000EVM is connected to the AWR1642BOOST with a ribbon cable which in turn, powers the device

through the same 5V power supply. Connection is required through another micro-USB cable for mmWave Studio to recognize the device.

3.2.1 mmWave Studio

In this section, the mmWave Studio interface will be explained in detail. mmWave Studio is a Graphical User Interface (GUI) that allows the user to customize the SDR for personal applications. This is the interface that produced the .bin file that was demonstrated earlier in Section 2.3.

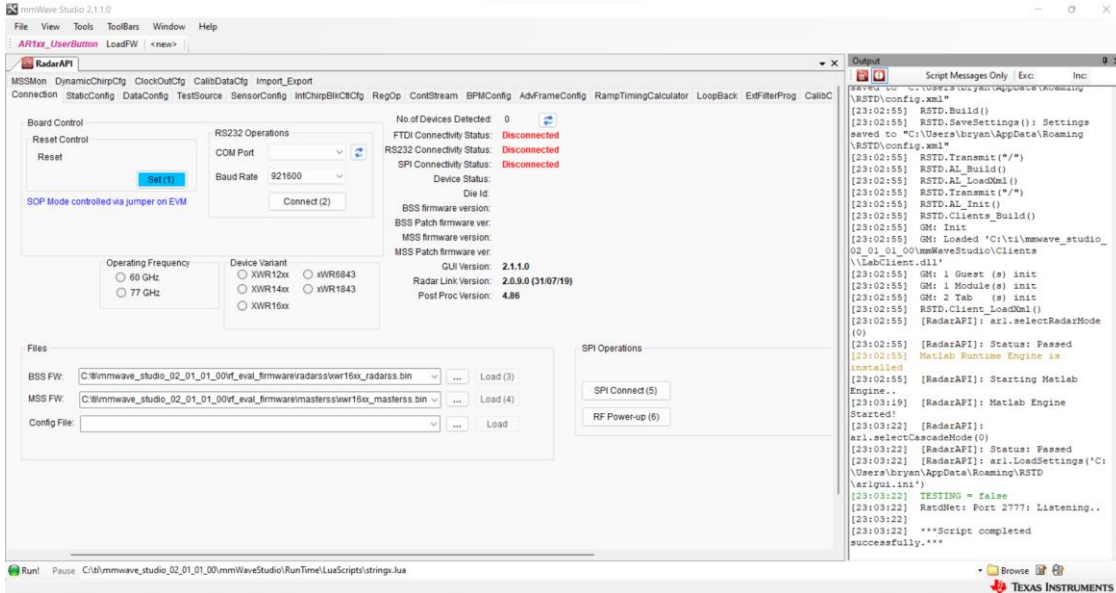


Figure 17: mmWave Studio connection setup.

Figure 17 shows the home screen after opening mmWave Studio GUI. The RadarAPI contains the different tabs for customizing the SDR configurations. The right side contains the output of script messages, notifying the user when a task is performed or when an error occurs.

In the connection setup tab of mmWave Studio, the connection is established between the SDR and the laptop. This involves resetting the board controls, selecting the correct COM port, flashing the BSS and MSS files, and connecting the SPI to power the system. After the system is connected and powered, the static configuration is set up through the layout shown in Figure 18.

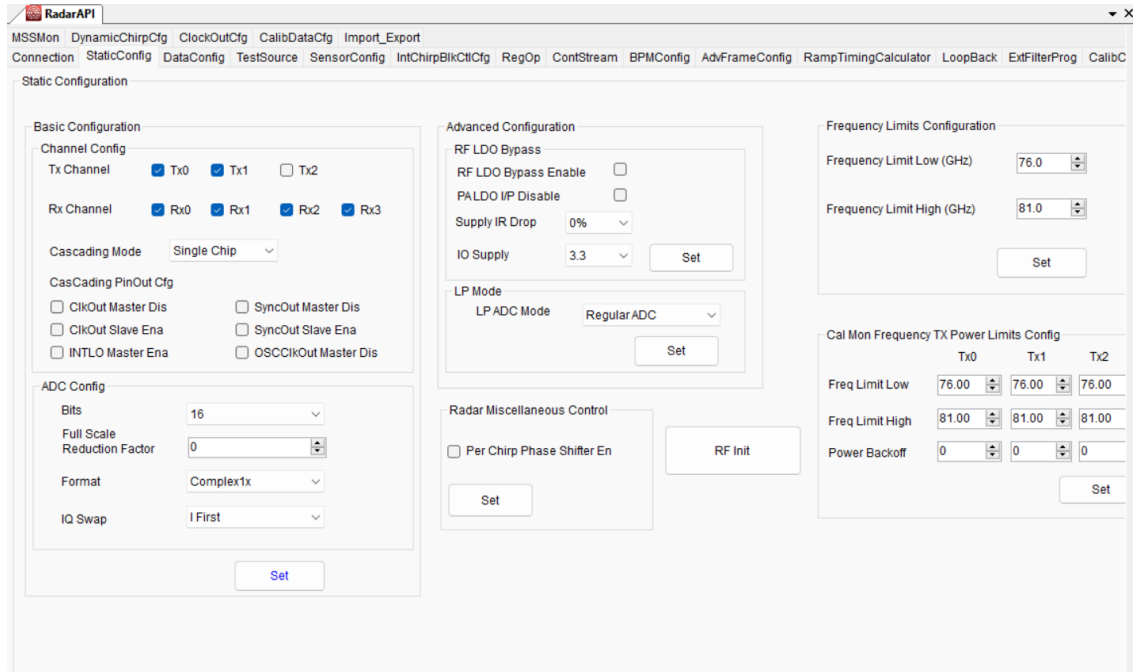


Figure 18: mmWave Studio static configuration window.

In the static configuration tab, the number of channels for the antennas can be customized. The AWR1642BOOST + DCA1000EVM can support up to two transmit channels and four receive channels. Within this tab, the ADC format is also configured.

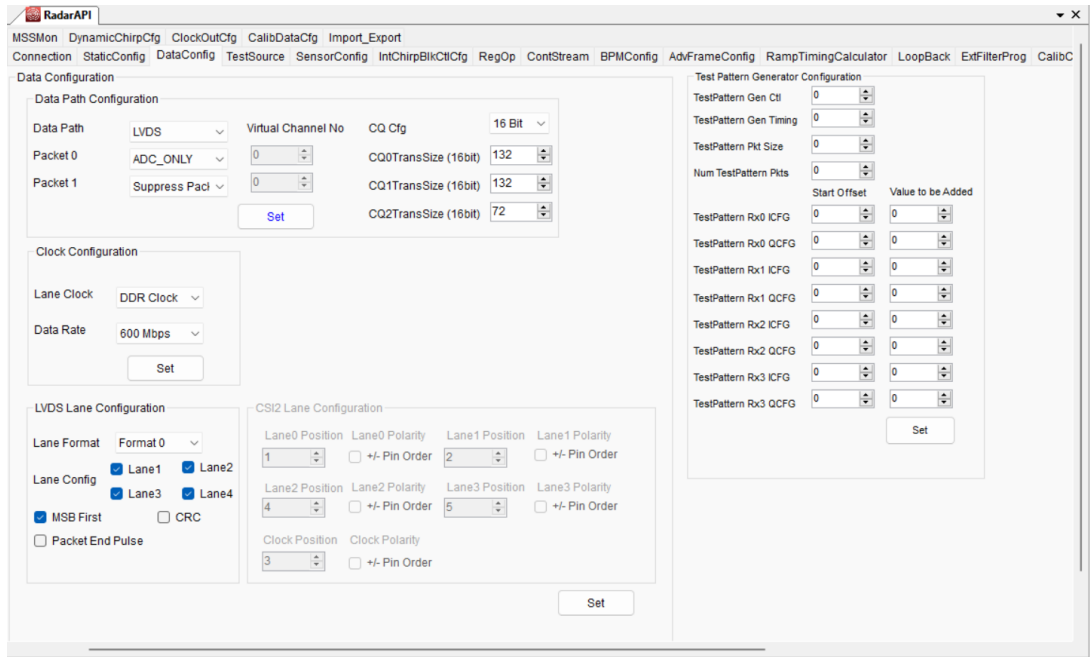


Figure 19: mmWave Studio data configuration window.

Figure 19 shows the data configuration tab. The format that the output .bin file is written can be adjusted here. More information can be found in the mmWave Studio GUI User Guide.¹⁰

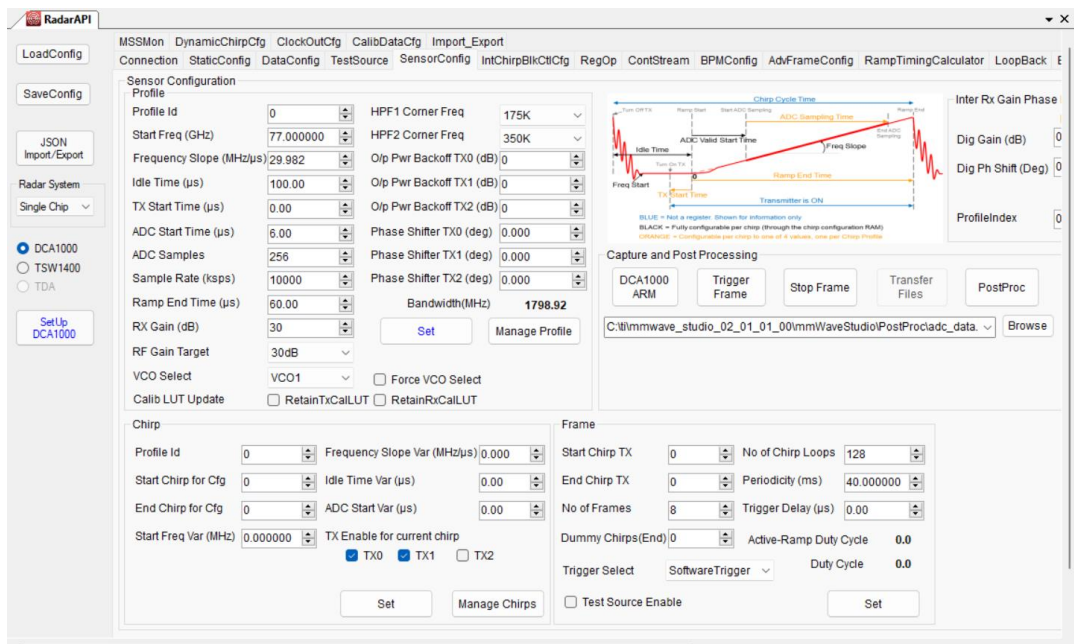


Figure 20: mmWave Studio sensor configuration window.

Figure 20 is the sensor configuration tab, where the parameters of the SDR are set for custom experimental design. This includes variables like the frequency, frequency slope, ADC samples, and other parameters that affect the chirp. The frame section allows for Doppler characteristics as it uses multiple chirps for velocity measurements.

Although mmWave Studio allows the user to optimize the values, limitations are set by the hardware that is used for the task. For an AWR1642BOOST + DCA1000EVM combination, customizable limitations for critical parameters are shown in Table 4.

Table 4: SDR radar parameters.

Parameter	Value
Start frequency	76 – 81 GHz
Bandwidth	0 – 5 GHz
ADC samples per chirp	64 – 256
Sample rate	2 – 6.25 Mbps
Chirp time	25.6 – 200 us
Chirps per frame	64 – 255

Lastly, the Capture and Post Processing section allow the user to collect data. The output path is selected, and the user will find the .bin file output. Before recording, DCA1000 ARM is clicked to ping the device. After a couple of seconds, pressing Trigger Frame will begin recording. The recording can be stopped manually by selecting stop-frame; otherwise, the LUA shell output will notify the user that the recording has been completed. After the recording is completed, the post-processing button can be utilized which will operate mmWave Studio's post-processing features shown in Figure 21.

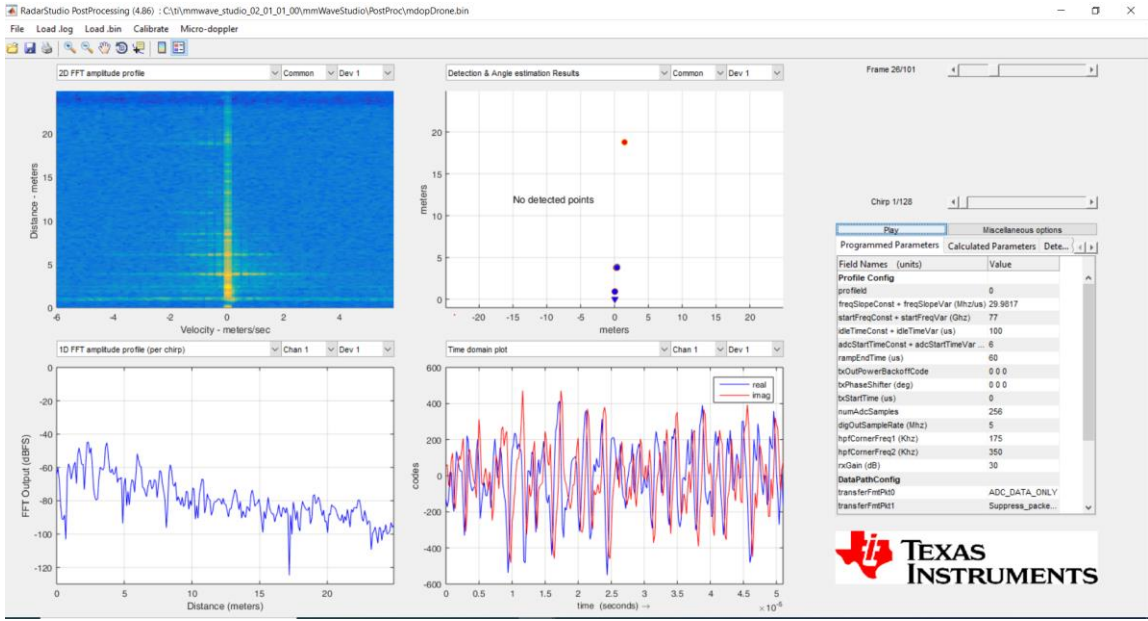
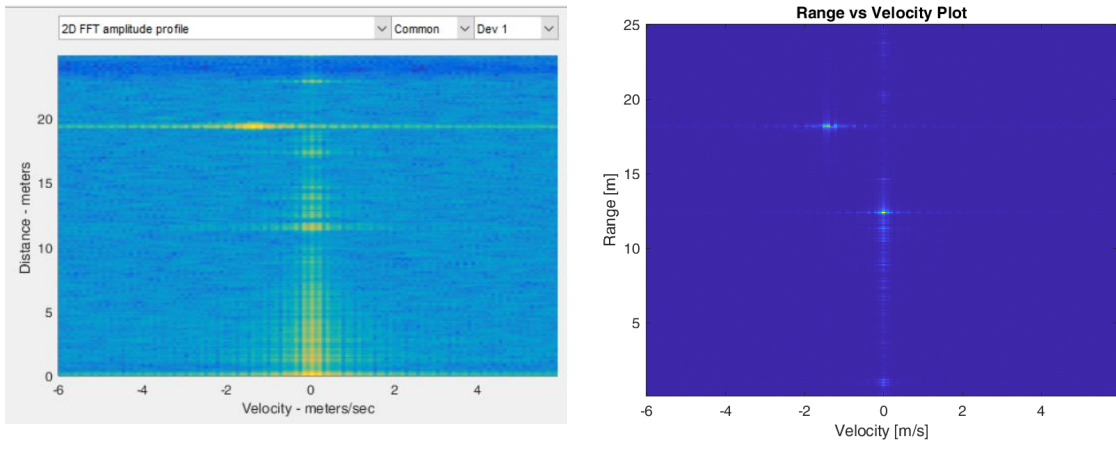


Figure 21: mmWave Studio post-processing.

Within the post-processing window, many visualizations are possible. The .bin file being read is shown at the top. The frame and chirp visualized are displayed at the top right side with the radar parameters shown underneath. Four plots can be shown at the same time. In addition, previous recordings can be accessed by loading the .log and .bin files.

Lastly, range-velocity maps are generated and compared with the results in mmWave Studio's post-processing 2D FFT amplitude profile space. These are similar and accurately depict the target's range and velocity at a given time, as seen in Figure 22.



a) mmWave Studio

b) MATLAB

Figure 22: Corner reflector range-velocity map comparison.

Additionally, mmWave Studio also contains a constant stream tab that simulates a continuous wave radar. This transmits a single frequency and only collects Doppler data, although it is very buggy. Many of the issues are discussed on the TI online forums but have not been resolved. The window for the constant stream tab is shown in Figure 23.

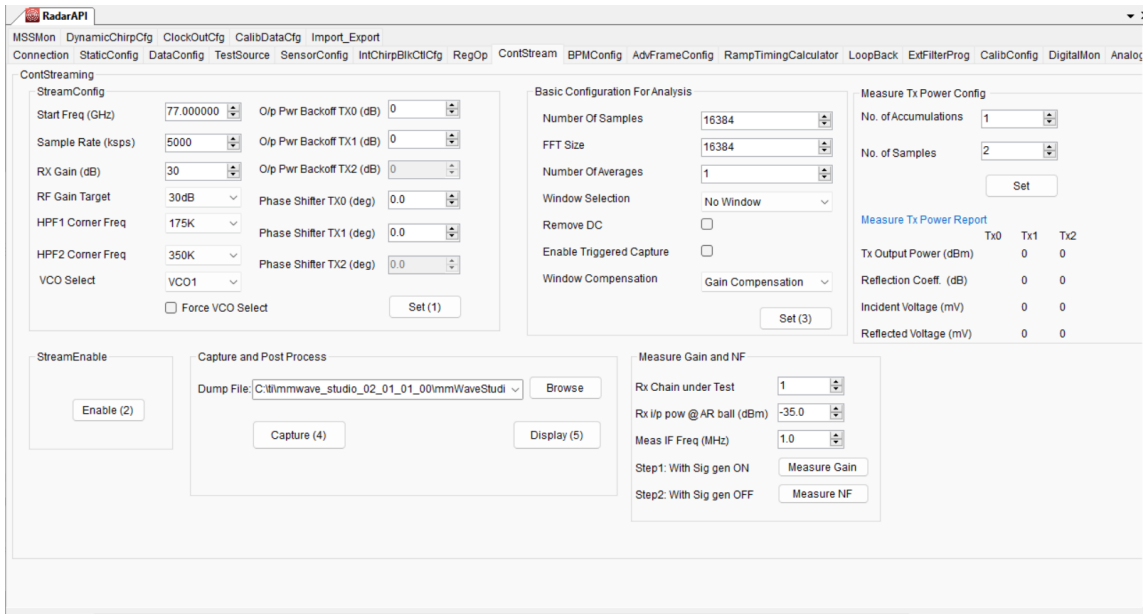


Figure 23: mmWave Studio constant stream tab.

Although the constant stream window simulates a CW radar signal, given the sampling rate and frequency of the device, the output file size is massive. This tab was not explored deeply due to time constraints.

3.3 Radar System Limitations

The radar limitations played a large role in the fluency of experiments conducted throughout this thesis.

3.3.1 10-GHz Radar Limitations

Starting with the 10-GHz system, the performance of micro-Doppler detection suffered due to hardware imperfections. The voltage-controlled oscillator was measured with a spectrum analyzer and was shown to have a lower power output than expected by roughly 6 dB. More importantly, I/Q imbalance was a major undesirable limitation in the overall performance of the 10-GHz system.

I/Q imbalance is an undesired side effect of hardware imperfections. Due to the inconsistencies between devices throughout the system, the amplitude and phase shift between the in-phase and quadrature signal most likely will be offset even though it is expected to contain a similar amplitude at a 90° phase shift. Some likely causes of this effect may be phase errors or distortions in the coaxial cables. The I/Q mixer may also be at fault.

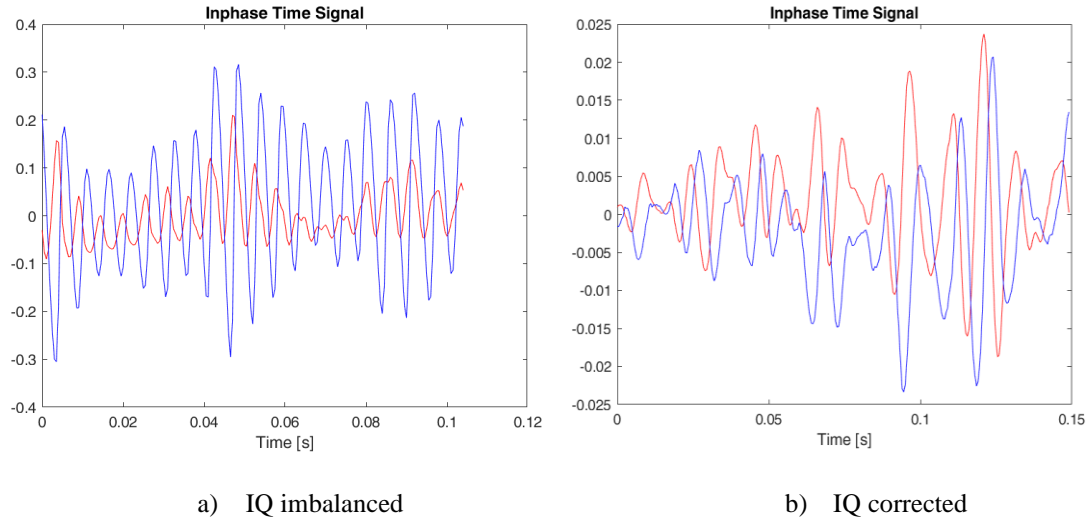


Figure 24: I/Q time signal plots.

In Figure 24, the in-phase signal, shown in red, has a weaker amplitude than the quadrature signal. In addition, the phase shift is not exactly at 90° . This was corrected by increasing the amplitude and shifting the signal by several samples corresponding to a full 90° .

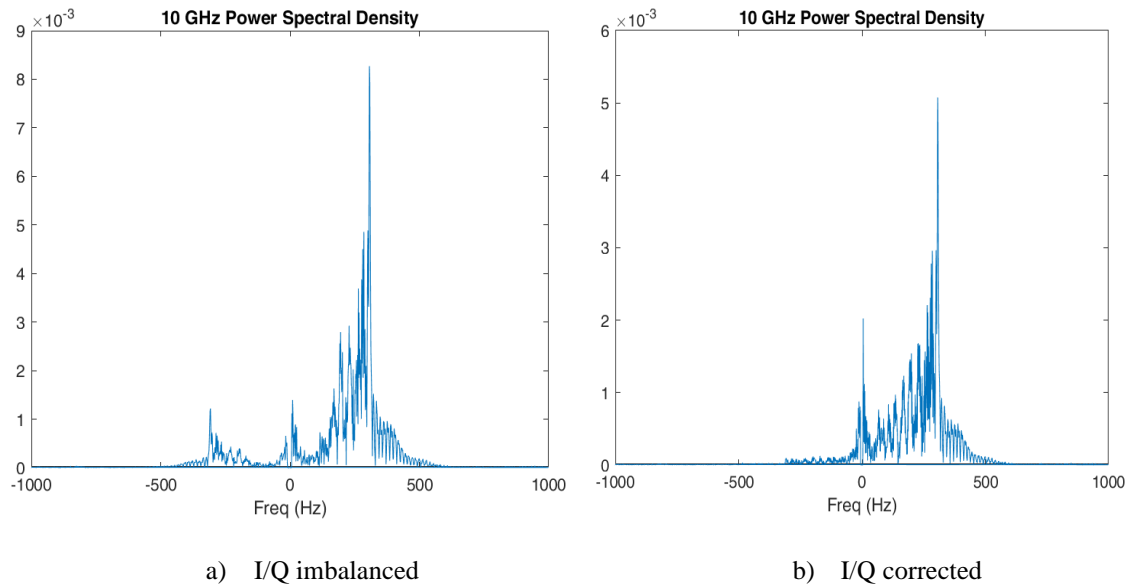


Figure 25: FFT power spectral densities before and after I/Q correction.

In Figure 25, the power spectral density is shown, displaying the Doppler frequencies before and after I/Q correction was applied. The negative frequencies were suppressed significantly while the positive frequencies maintained a dominant presence. In terms of filtering out undesired frequencies, this is not so simple since the micro-Doppler motions of the target span across the range of frequencies that were in consideration for filtering.

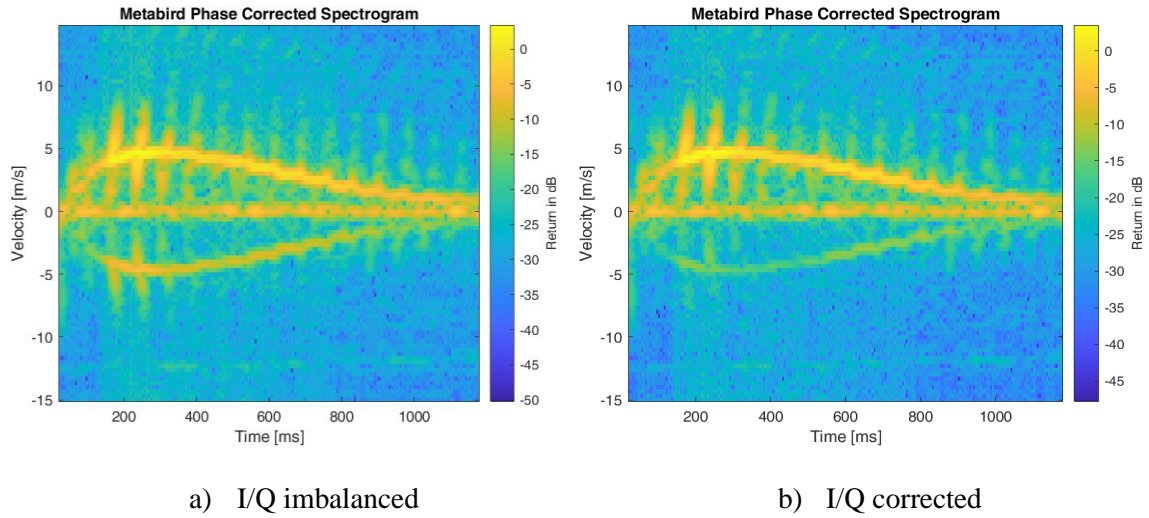


Figure 26: Spectrograms before and after I/Q correction.

Figure 26 displays the spectrograms of a Metabird (small bird-like UAV) flight before and after I/Q correction was applied. Micro-Doppler from the reflection in the negative velocities is present in both, but after the phase was adjusted, the reflection is much weaker. Unfortunately, the main body is still reflected, although not as strong.

3.3.2 77-GHz Radar Limitations

Although the 77-GHz device was impressive in terms of the applications possible, there are many limitations associated with the SDR. A large limitation was the incoherency within the documentation when learning how to operate the device. Many of the tutorials were unfunctional

and the documented performance was not supported by the true device operability. For example, the sampling rate should be operable up to 10 MHz, but the maximum is 6.25 MHz. When trying to troubleshoot the device, the online forums did not provide much help, as many of the posts were outdated or poorly answered. In addition, a lot of time was spent trying to replicate the post-processing window in mmWave Studio into MATLAB. One of the largest limitations of the device is that the high frequency meant a large sampling rate was required. This resulted in extremely large file sizes, counter-productive for ATR.

Chapter 4 – Experimental Results

4.1 – Simulation Setup

Before data were collected experimentally, simulations were created to replicate the micro-Doppler detection scenario. These simulations are created in the MATLAB environment by using the Radar Toolbox. The Radar Toolbox expedites and supports the simulation of radar systems from the design, deployment, and field data analysis. First and foremost, constants are set for the initial simulation parameters. The simulation parameters are given in Table 5, denoting the setup for the drone behavior throughout the detection process.

Table 5: Simulation parameters.

Simulation Parameter	Value
Environment	Free space
Range	10 m
Dwell time	0.5 s
Sampling rate	12 kHz
Drone Parameter	
Number of rotors	4
Blades per rotor	2
Average blade rotation rate (ω)	56 revolutions per second
Blade length	0.1 m
Radar cross section	0.3 m ²

The drone that was used in this simulation is the AKASO A31 medium-sized quadcopter. The physical characteristic of this UAV is given in Table 6, along with the other UAV parameters in Section 4.3.

By using the phased toolkit, a rectangular waveform is used to simulate the CW behavior of the 10-GHz signal. The sampling rate and the Pulse Repetition Frequency (PRF) are at the same value of 44.1 kHz, the default sampling rate of a laptop's audio card. By setting the sampling rate and the PRF to the same value with the pulse width equal to the inverse of the PRF, a 100% duty cycle is simulated.

Two antenna elements are used, one for transmit and one for receive. These antenna elements are spaced at a half-wavelength (i.e., $\lambda/2$) distance apart from each other. The transmit power used was 70.79 mW with a gain of 22 dB. The receiver preamp was set to a gain of 19 dB and a noise figure of 1.7 dB. The environment is free space where the propagation speed is the speed of light.

The drone body is positioned at (10,0,10) where the z-axis is the height. The target velocity is 0 for all axes, meaning the drone is hovering in place. The drone behavior is simulated by consisting of the main body RCS of 0.3 m^2 with 4 accompanying motors each evenly positioned 15 cm away from the body.

A for loop is created to simulate each ‘pulse’, sample. With each sample, the drone and each blade position are updated. The sample is transmitted to the target and reflected on the radar. The value is stored in an array until each sample is transmitted and received, summing up to 0.5 seconds.

The first plot generated is a time plot shown in Figure 27. This represents the raw values collected by the radar system.

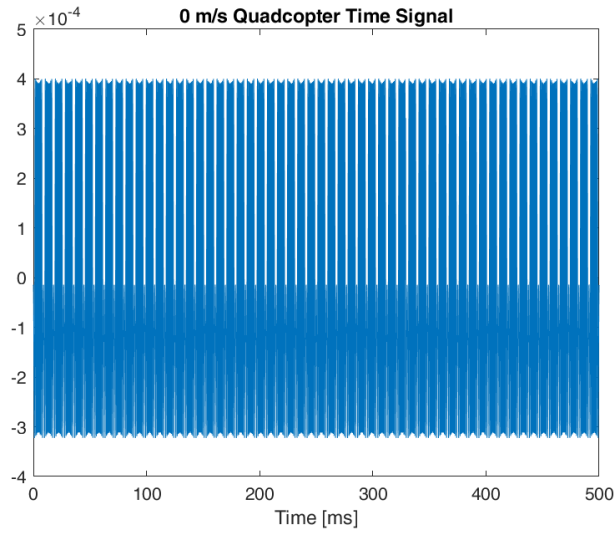


Figure 27: Simulated quadcopter time signal.

Following, the FFT is performed on the time signal. Since the FFT is a cyclical process, the frequency axis is split into negative and positive frequencies. The frequency axis is converted to velocity using equation (1). The frequency response is shown in Figure 28.

The maximum detectable velocity is around ± 30.24 m/s but the strongest return is at ± 23.52 m/s.

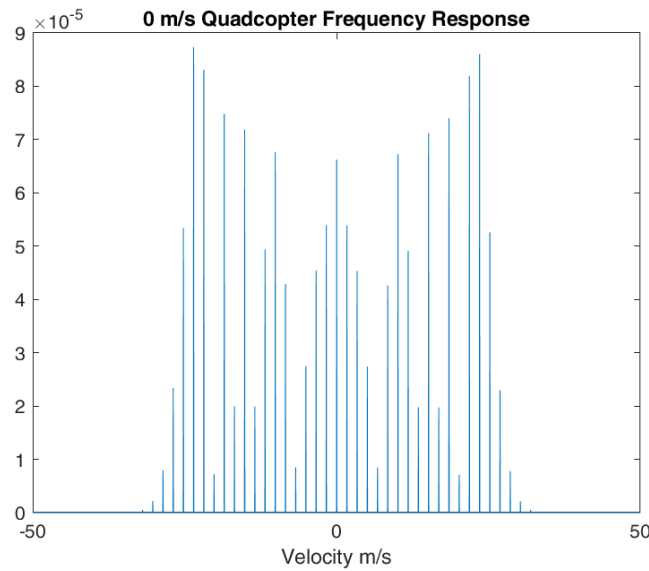


Figure 28: Simulated quadcopter frequency response.

Lastly, spectrograms are generated with a window size of 128 segments with 120 overlapping segments. The time axis, originally in seconds, is converted to milliseconds. The frequency axis is converted to velocity.

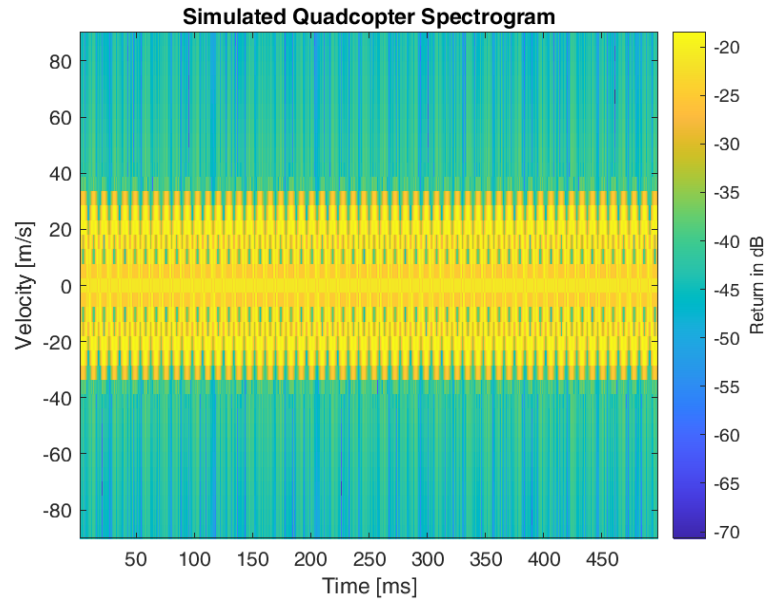


Figure 29: Simulation quadcopter spectrogram.

The spectrogram in Figure 29 accurately displays the micro-Doppler signature of a hovering quadcopter. Periodic maximum velocity values are visible, confirming the cyclical nature of the rotating blades.

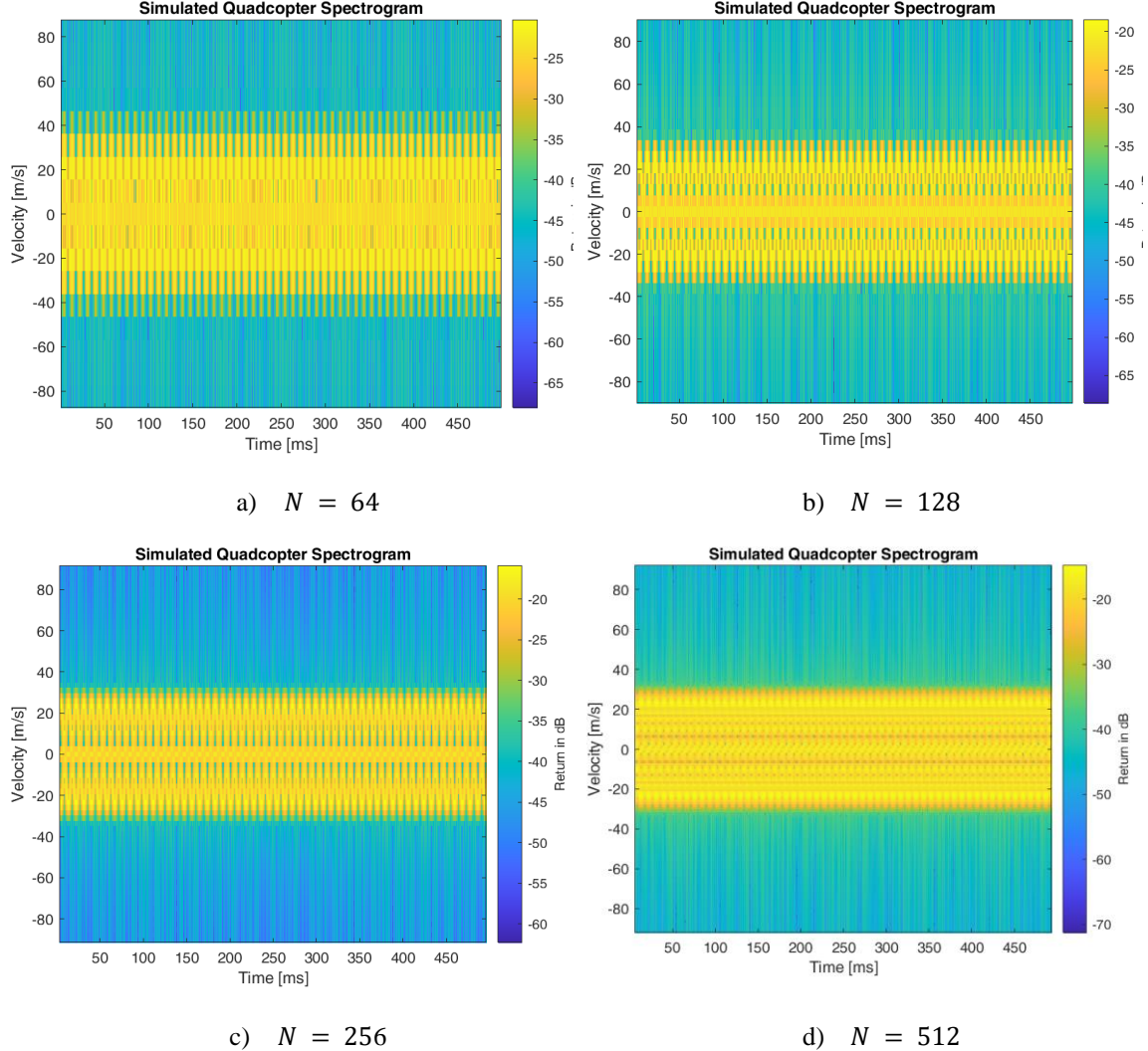


Figure 30: Spectrograms with different window sizes.

Figure 30 shows simulated spectrograms with different window sizes. By adjusting the window size of the STFT, the tradeoff between the time resolution and Doppler resolution is witnessed. When the window size is set to 64 samples, the time resolution is very fine, emphasizing the micro-Doppler periodicity of each blade tip. But the velocity readings span a range of values that result in ambiguity regarding the true Doppler velocity. On the other hand, with a window size of 512 segments, the time resolution becomes ambiguous, but the velocity

measurements are finer and more precise. For the images generated for the datasets in this work, a window size of 128 segments was utilized.

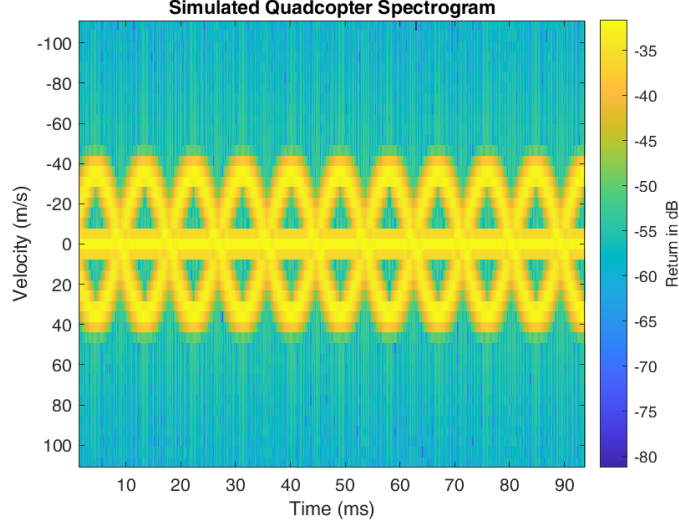


Figure 31: Simulated quadcopter results (shortened integration time).

In Figure 31, the integration time is lowered to emphasize the periodicity within the blade rotations. Peaks are detectable around ± 40 m/s.

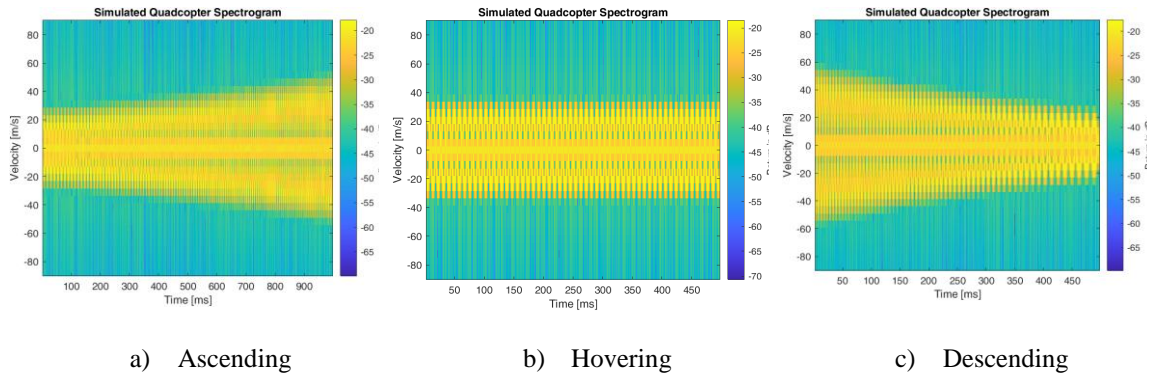


Figure 32: Different rotation accelerations.

In Figure 32, simulations are generated to replicate the ascending, hovering, and descending motions of a quadcopter. By increasing the acceleration of the blades through time,

the simulation mimics the vertical motions of a quadcopter. Given more time, simulations could have been performed to imitate a quadcopter moving in translational directions. Although, there is much more complexity involved when considering rotor mechanics to account for roll, pitch, and yaw.

4.2 – Data Collection Process

Drone data were collected both indoors and outdoors. The recording process was similar for both scenarios, but the setup was different.

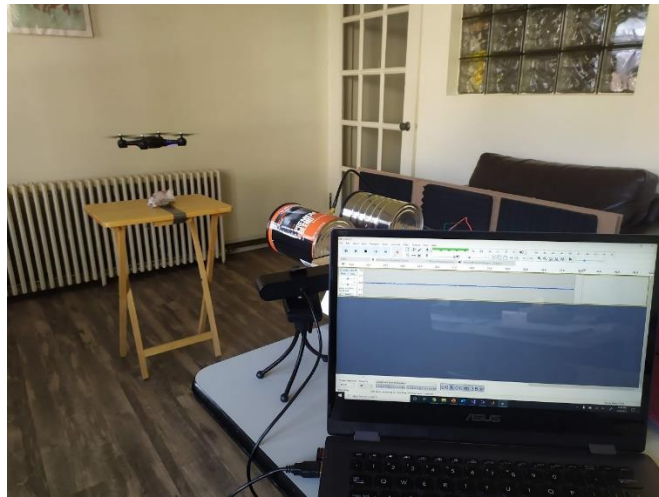


Figure 33: Initial indoor quadcopter micro-Doppler detection test.

Figure 33 shows initial indoor tests for recording real data with a quadcopter. The 10-GHz radar system is recorded through Audacity and verified with the webcam using PSI Studio.



Figure 34: Stationary drone data collection setup.

Figure 34 shows the physical setup of the indoor UAV experimental collection process. The quadcopter is held down to a table by using a fishing line and a bag of quarters to keep the tape attached to the table as the drone flies.



Figure 35: Outdoor drone data collection setup.

Moving outdoors, most of the data were collected by placing the drone 3-15 meters away from the radar system and performing different flight motions, as shown in Figure 35. There were

a few difficulties when trying to obtain the micro-Doppler signatures of the drones. The RCS of the blades was too low that methods for increasing the detectability were conducted.



Figure 36: Akaso UAV with reflective tape on the blade tip.

Micro-Doppler was enhanced by adding reflective tape onto the blade tips of the quadcopter rotors, as shown in Figure 36. This significantly improved the detectability.

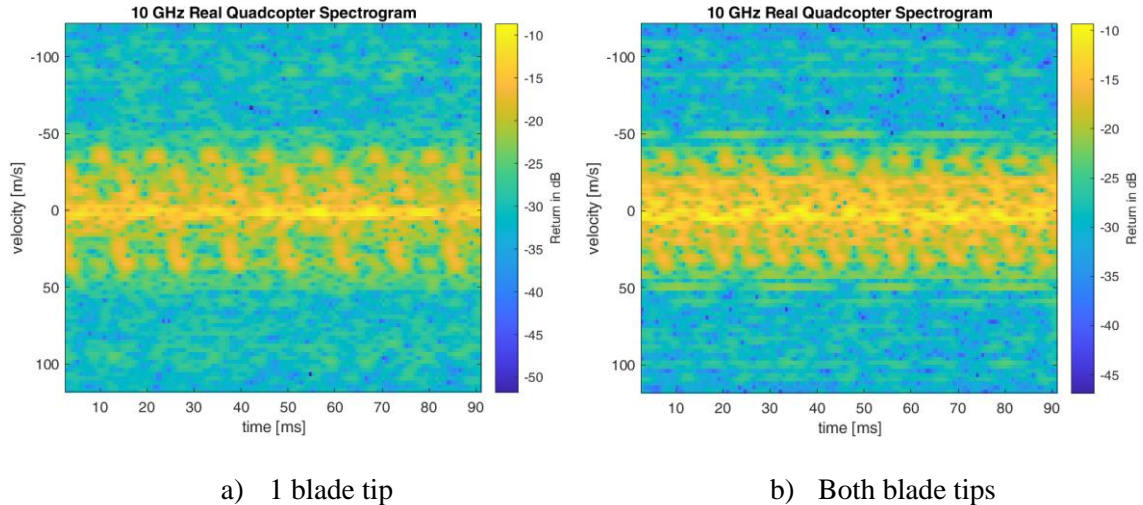


Figure 37: 0° LOS reflective tape on a rotor.

In Figure 37, spectrograms are generated based on real data with a 0° line of sight. The first image contains reflective tape on a single blade tip (1/8) while the second shows 1 rotor, 2 blades, taped with reflective tape.

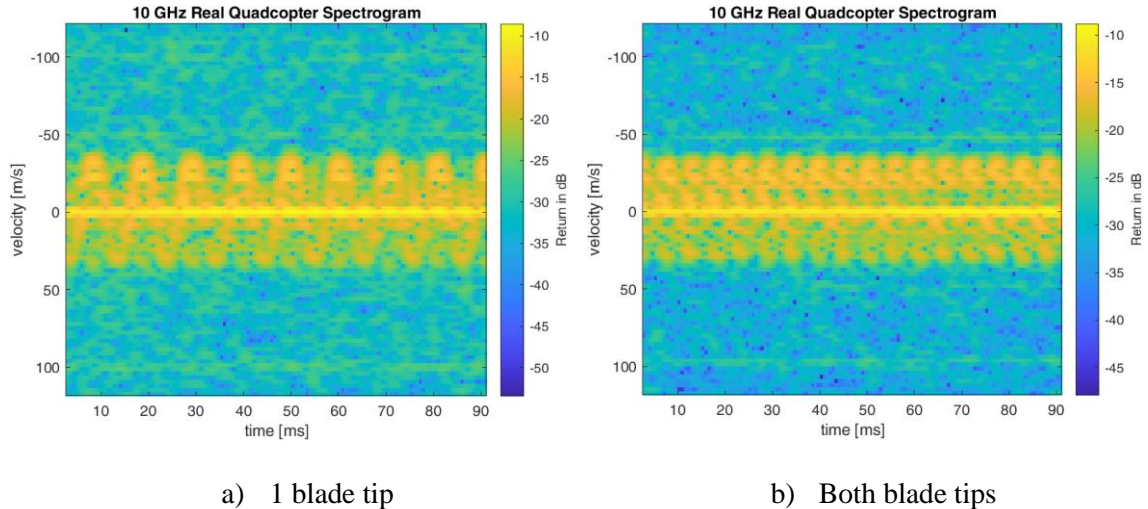


Figure 38: 30° LOS reflective tape on a rotor.

In Figure 38, a similar experiment is performed except with a 30° LOS. This pronounces the micro-Doppler pattern since the overall RCS of the blades is increased.

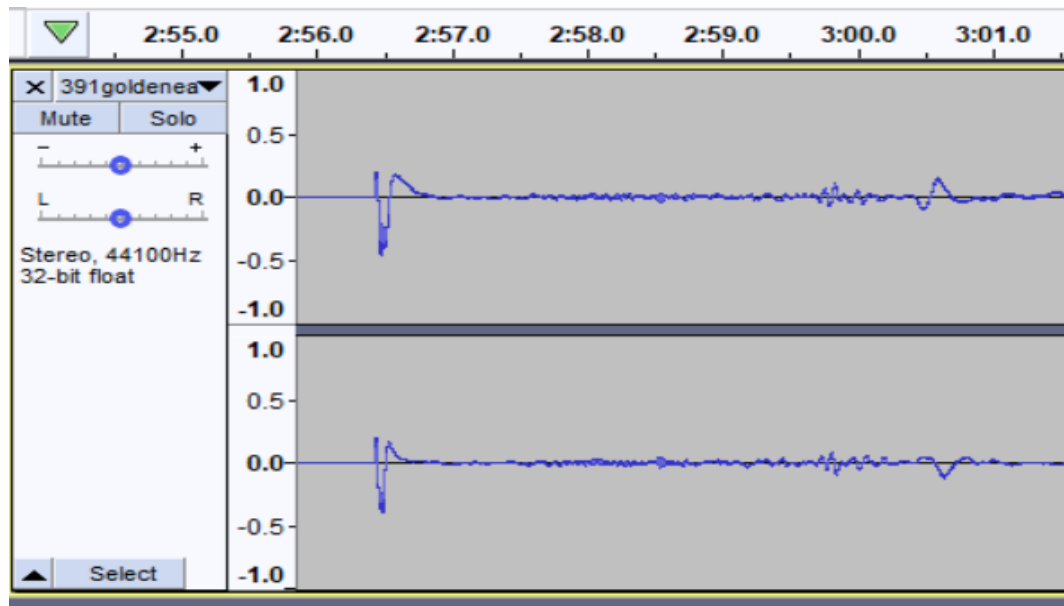


Figure 39: Recorded raw data in Audacity.

As mentioned previously, data were collected within Audacity and stored as a .wav file. Before the flights, recording begins in Audacity shown in Figure 39. After this, the radar system begins recording by turning on the power supply. This introduces a timing mark in both audacity and PSI Studio to notify the user when recording begins.



Figure 40: PSI Studio for ground truth.

PSI Studio is used as ground truth which allows the user to align the audio segment with Audacity and review the video stream recorded through the webcam, as seen in Figure 40. PSI Studio is a powerful tool, created through C# that allows for offline and live visualization of recording. A con of using PSI Studio for visual ground truth is that flight requires a significant amount of memory.

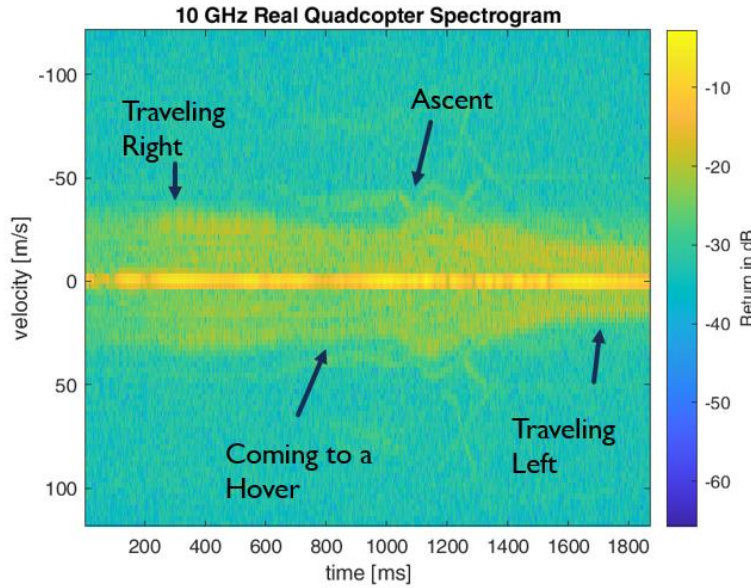


Figure 41: Generated Spectrogram in MATLAB based on raw data.

Figure 41 shows the generated spectrogram of a quadcopter flight over 2 seconds. The behavior of the UAV is verified through PSI Studio's video footage. At the start of the spectrogram, the UAV travels to the right at full speed. The micro-Doppler bandwidth decreases as it comes to a hover in place. Shortly after, the UAV ascends, and the micro-Doppler bandwidth increases again. The UAV returns to a steady altitude and begins to descend, and travel left as the spectrogram ends.

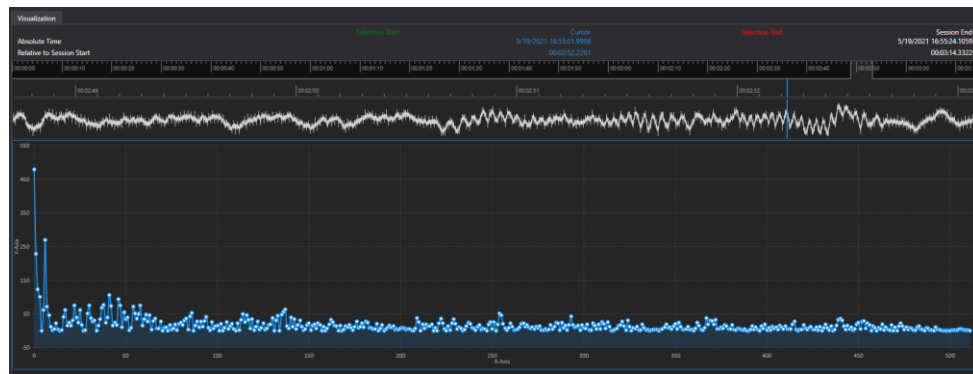


Figure 42: PSI Studio FFT feature.

PSI Studio also can perform FFT on the audio clips, as seen in Figure 42. This feature was not explored deeply since the rendering time was significantly higher than using MATLAB. In addition, PSI Studio could not stream the FFT plot in real-time and it was also unable to display both the video recording and the FFT plot simultaneously. Another problem was that there was only a single channel available, so I/Q data was not possible. This is an issue that may have been resolved, given more time.

4.3 – UAVs

The description of each UAV is provided in Table 6.

Table 6: UAV characteristics.

Dimension	Metabird	Akaso Quadcopter	BlackHawk Quadcopter
Weight	10 gm (0.022 lb)	750 gm (1.65 lb)	1775 gm (3.87 lb)
Body Length	16 cm (6.3 in)	–	–
Wingspan	33 cm (13 in)	38.9 cm (15.3 in)	77.7 cm (30.6 in)
End-to-End Span	–	19.5 cm (7.7 in)	26.0 cm (10.2 in)
Blade Axis to Blade Axis	–	16.3 cm (6.4 in)	22.0 cm (8.7 in)
Blade Length	–	7.0 cm (2.8 in)	9.5 cm (3.7 in)
Height	–	10.5 cm (4.1 in)	12.0 cm (4.7 in)

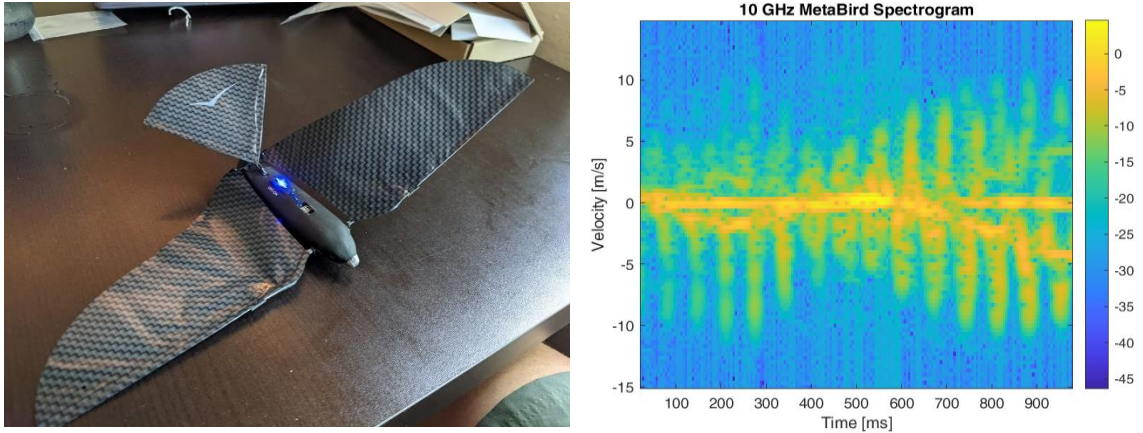


Figure 43: Metabird (small) and its associated spectrogram.

Figure 43 shows the smallest UAV, a Metabird, and its spectrogram. The micro-Doppler signature of the Metabird consists of periodic flaps of consistent velocities. The body has an undulating nature as it flies. The Doppler bandwidth changes over time due to the rotational behavior of the UAV. The Metabird does not always travel perpendicular to the radar.

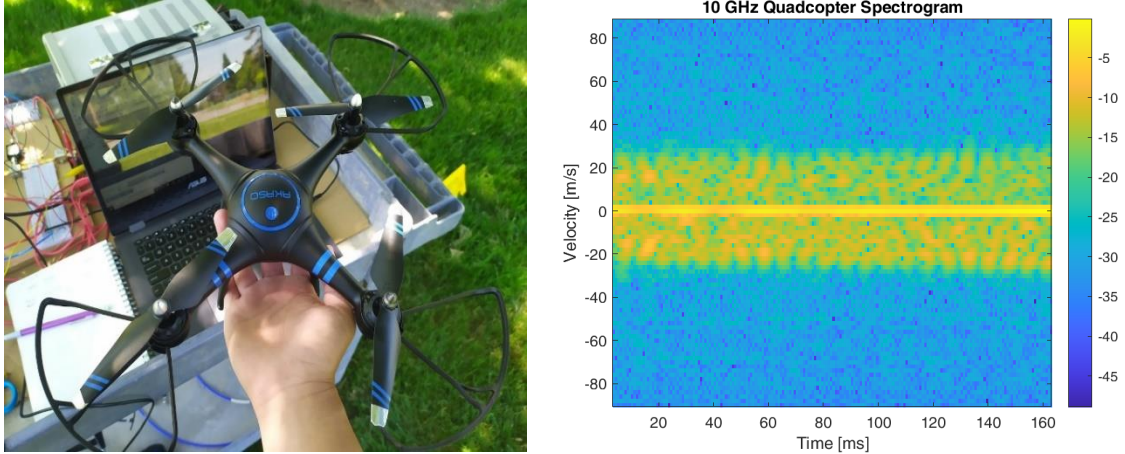


Figure 44: Akaso drone (medium) and its associated spectrogram.

Figure 44 shows the medium-sized, Akaso drone and its associated spectrogram. In this spectrogram, periodic shapes are present that are like the simulations. This spectrogram shows the

behavior of a drone slowly descending in the vertical direction. This is observed through the maximum velocity of the blade tips around 26 m/s.

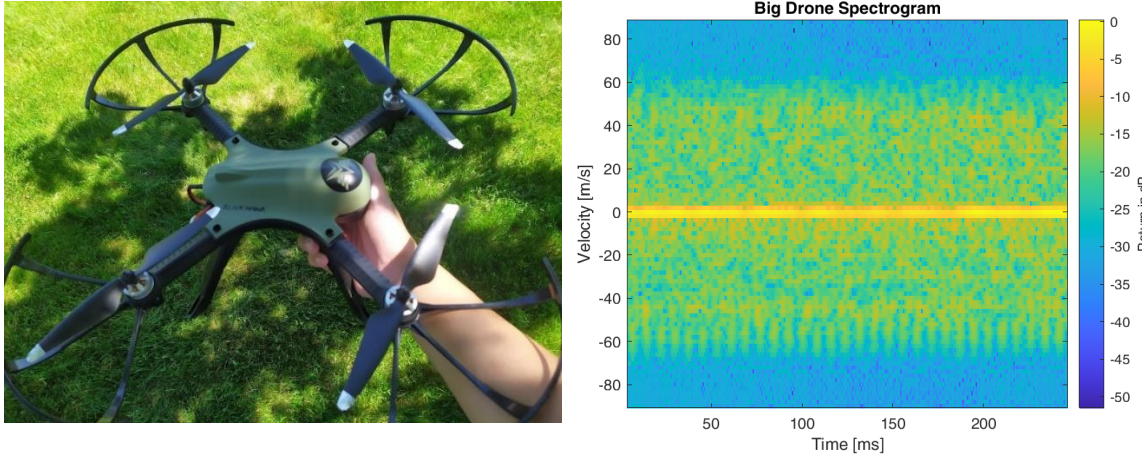


Figure 45: BlackHawk drone (big) and its associated spectrogram.

Figure 45 shows the large BlackHawk drone and its associated spectrogram. The maximum blade tip velocity is much higher compared to the Akaso drone. This is due to the overall weight of the UAV being higher than the Akaso. It is noticeable that the negative velocities show more pronounced micro-Doppler peaks compared to the positive side. This is because the positive peaks are hidden behind the arms of the drone, concealing the sharp micro-Doppler pattern.

4.3.1 – UAV Detection Scenarios

In addition to the data collected in free space, preliminary experiments were conducted with the Akaso drone to measure the effects of different situational micro-Doppler detection scenarios. The first measurement setup is shown in Figure 46.



Figure 46: Outdoor against-the-wall setup.

More real-world experiments were collected such as micro-Doppler detection in front of a metal barricade. It was of interest to compare the detectability of a UAV in front of a wall to investigate how the background affects the micro-Doppler signature compared to free space. In this experiment, the drone was placed 3 meters away from the radar system, directly in front of the wall. A flight was performed with the UAV moving in a variety of motions.

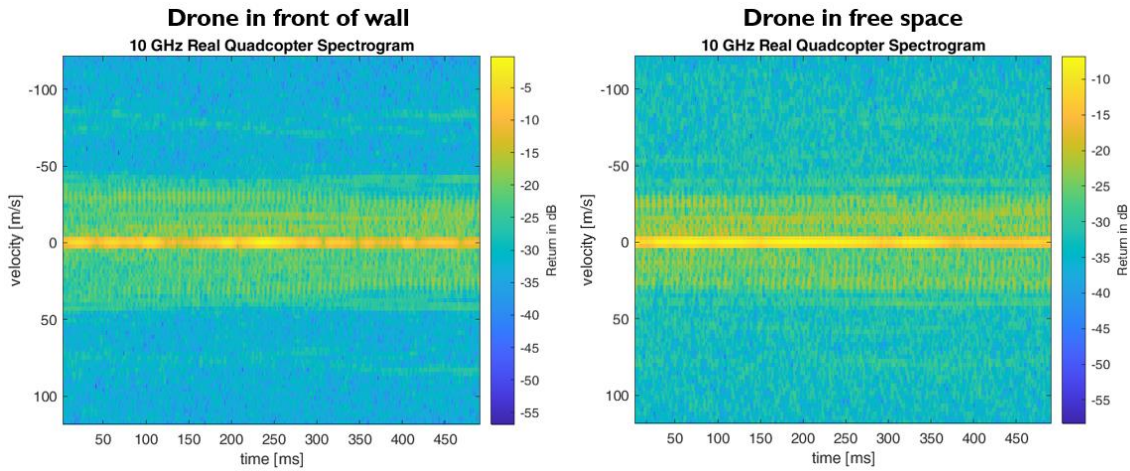


Figure 47: Wall vs. free space spectrogram comparison.

Figure 47 shows the comparison between spectrograms of the Akaso (medium) quadcopter in front of the wall vs. in free space. Overall, there is minimal difference between the two spectrograms.



Figure 48: Around-the-corner UAV detection.

Figure 48 shows the process and setup for around-the-corner micro-Doppler detection. Micro-doppler was detectable but significantly weaker than free space, as shown in Figure 49.

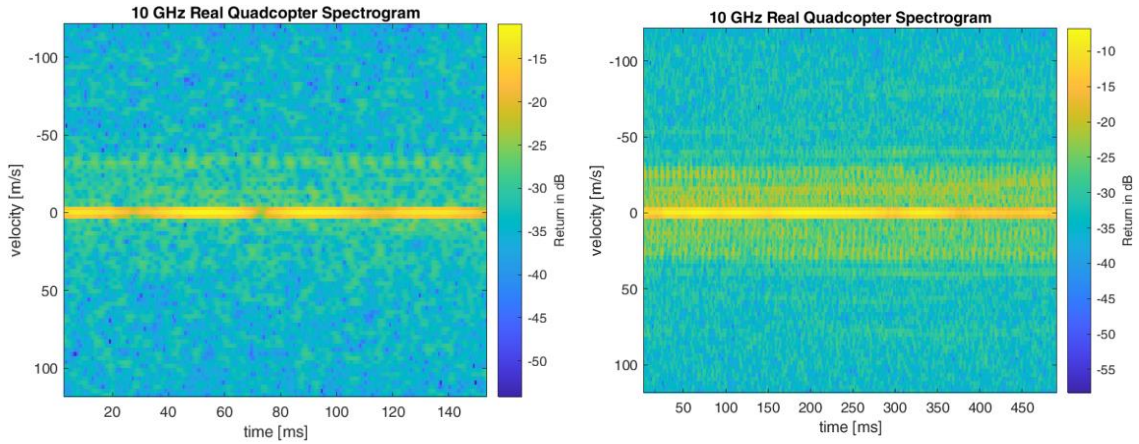


Figure 49: Around-the-corner vs. free space spectrograms.

The micro-Doppler signature was significantly weaker, with only the radial velocities closest to the bounced wall being detectable.

Another experiment that was conducted was detecting UAV micro-Doppler through tree foliage. Uniquely, the leaves on a tree contribute to additional Doppler frequencies.



Figure 50: Tree foliage UAV detection.

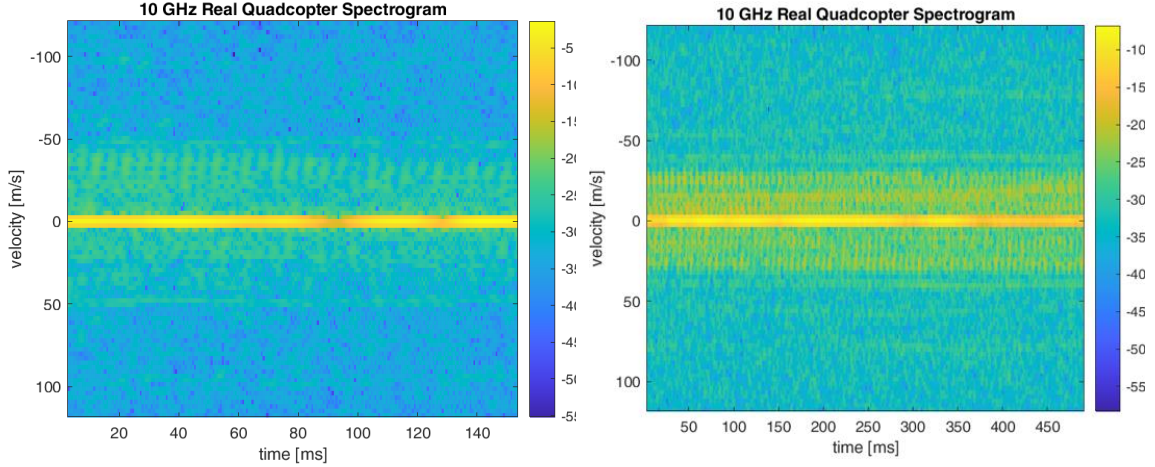


Figure 51: Tree foliage spectrogram.

Figure 51 shows the spectrogram of the UAV micro-Doppler signature through tree foliage. A similar effect to the around-the-corner experiment is present where the response is noticeably weaker than in free space.

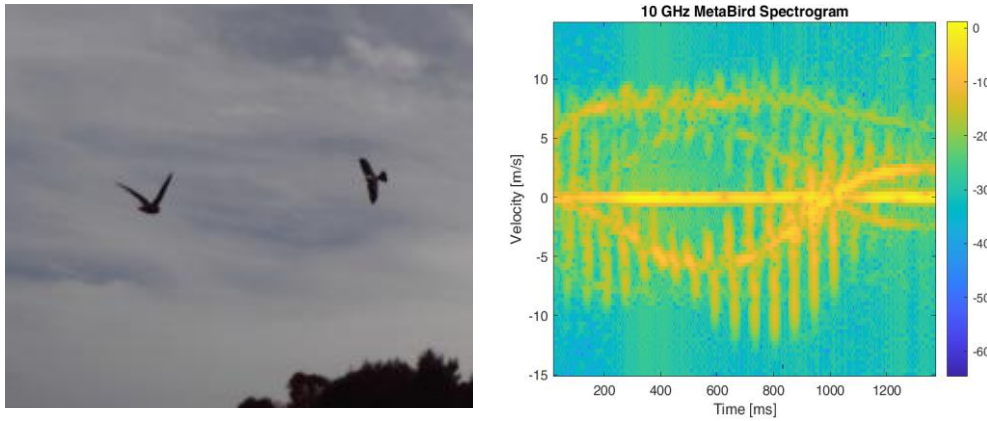


Figure 52: Metabird and real bird in the same recording.

In Figure 52, the Metabird was flown for data collection and an unexpected bird came into the LOS. The spectrogram is also shown in Figure 52.

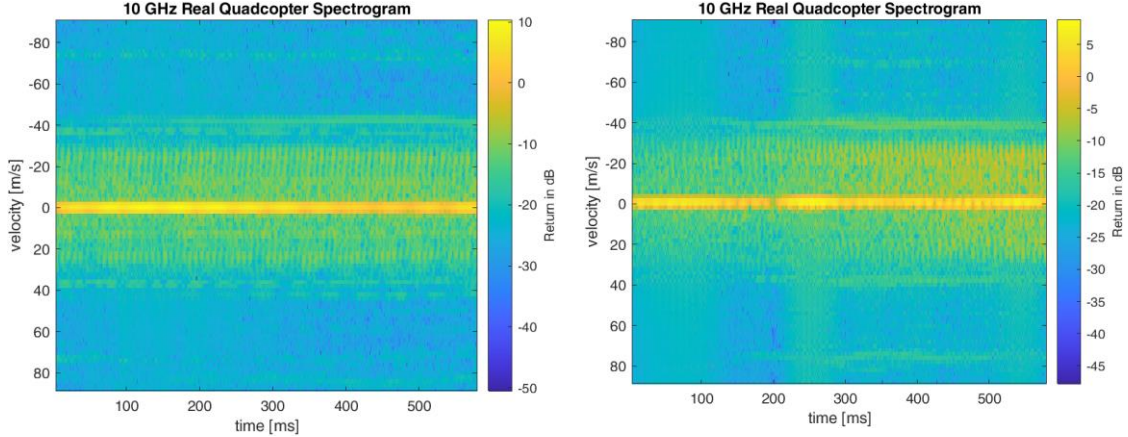


Figure 53: Stationary vs. rotating antenna UAV detection.

In Figure 53, a comparison is made between recordings when the antennas were stationary vs. rotating. For the rotating setup, the quadcopter hovers in a constant location while the antennas are swept. There is no significant difference between the two antenna setups.

4.4 – Birds

In this section, the setup for collecting data on birds is explained. Bird flights were collected with the 10-GHz radar at Shaver’s Creek, a bird sanctuary nearby Penn State University. Most of the birds at this aviary have a disability, but these did not significantly affect their flight patterns. Through the help of the trainers at Shaver’s Creek, birds flew from perch to perch, as the radar system recorded the Doppler shifts induced. The enclosure is wooden with wire meshing in between columns. Since the radar system only tracks radial movement, the enclosure does not play a role in the spectrogram quality. The reflections from the wall behind the bird did not affect its micro-Doppler signature. Although, this was not verified by a bird flight outside of the enclosure.



Figure 54: Bird data collection setup.

Figure 54 shows the bird enclosure and radar system. Four different birds were used in this experiment: bald eagle, golden eagle, broad-winged hawk, and American kestrel. The weight, length, and wingspan of each bird are provided in Table 7.

Table 7: Bird characteristics.

Physical Feature	American Kestrel	Broad-Winged Hawk	Golden Eagle	Bald Eagle
Weight	68 – 163 gm (0.15 – 0.36 lb)	340 – 454 gm (0.75 – 1 lb)	2.95 – 6.12 kg (6.5 – 13.5 lb)	3.00 – 6.30 kg (6.6 – 13.9 lb)
Length	21.0 – 31.8 cm (8.25 – 12.5 in)	34.3 – 44.5 cm (13.5 – 17.5 in)	69.9 – 83.8 cm (27.5 – 33 in)	71.1 – 96.5 cm (28 – 38 in)
Wingspan	50.8 – 61.0 cm (20 – 24 in)	81.3 – 101.6 cm (32 – 40 in)	1.83 – 2.13 m (6 – 7 ft)	1.83 – 2.29 m (6 – 7.5 ft)

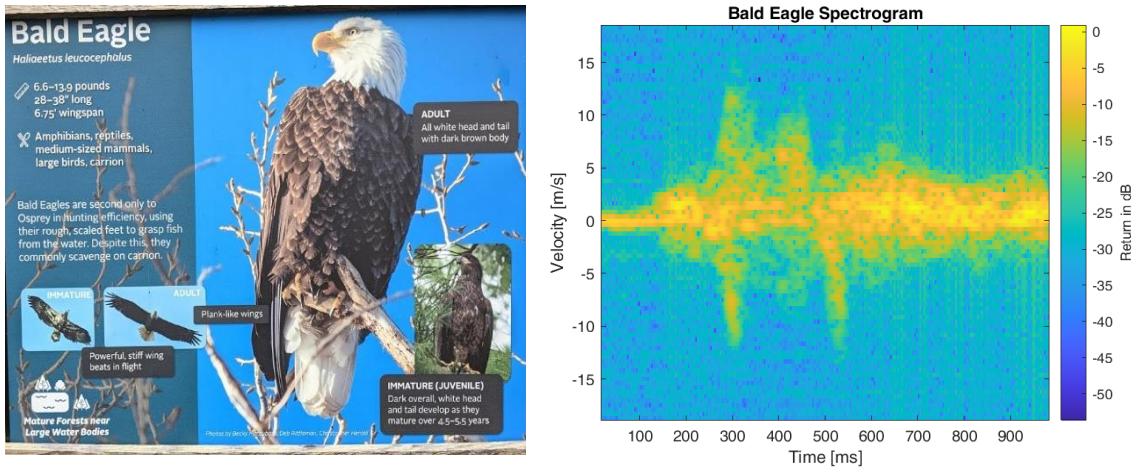


Figure 55: Bald eagle and its associated spectrogram.

Figure 55 contains the bald eagle spectrogram. Within this spectrogram, a large velocity bandwidth is initially witnessed at around 300 ms. This represents the downstroke of the bird, quickly followed by an up-flap. The back half of the spectrogram shows the soaring of the bird as it mechanically controls the rest of the flight.

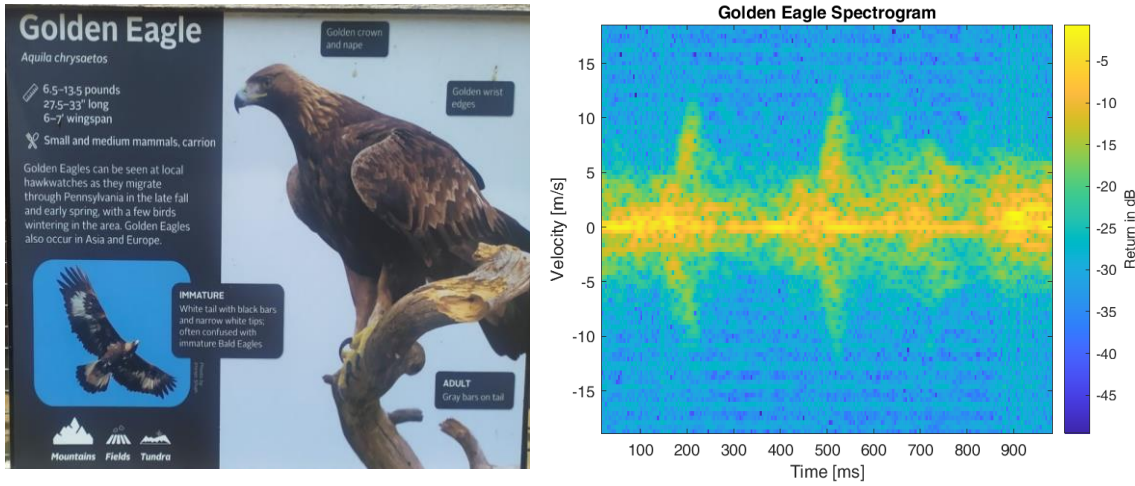


Figure 56: Golden eagle and its associated spectrogram.

Figure 56 contains the golden eagle spectrogram. The golden eagle spectrogram is quite like the bald eagle, with strong flaps present at 200 and 500 ms. Unlike the UAVs, the flapping is not consistently periodic, as flapping requires large amounts of energy. If the birds had a larger environment to fly in, the micro-Doppler signatures may look quite different since soaring would be more viable.

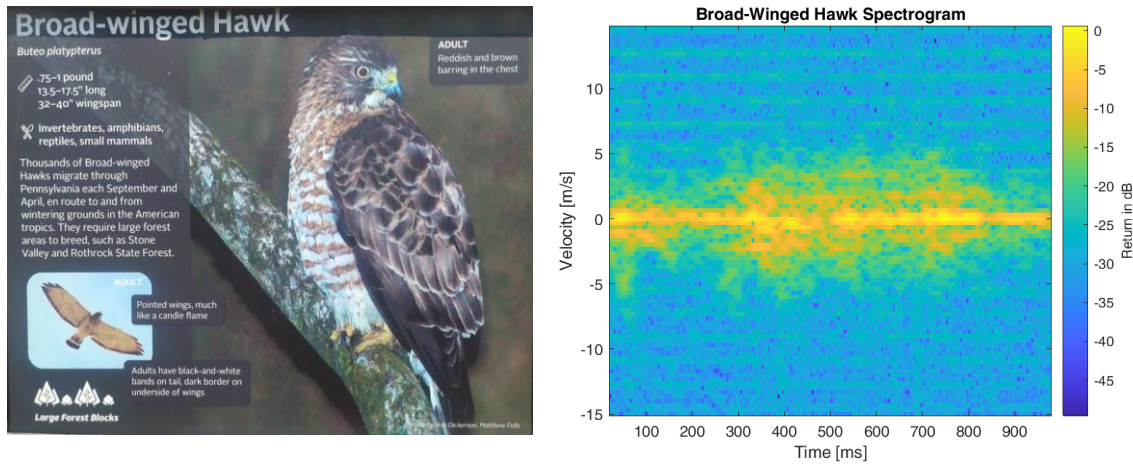


Figure 57: Broad-winged hawk and its associated spectrogram.

Figure 57 is the spectrogram for the broad-winged hawk. The broad-winged hawk is the second smallest bird. The smaller birds require a higher periodicity in flaps compared to the eagles, but their flaps do not need to be as strong since they are supporting a smaller payload. The micro-Doppler signature is quite cluttered since the body of the bird undulates. This makes the peaks of the wing flaps less pronounced. The maximum velocity achieved by the broad-winged hawk is around 5 m/s.

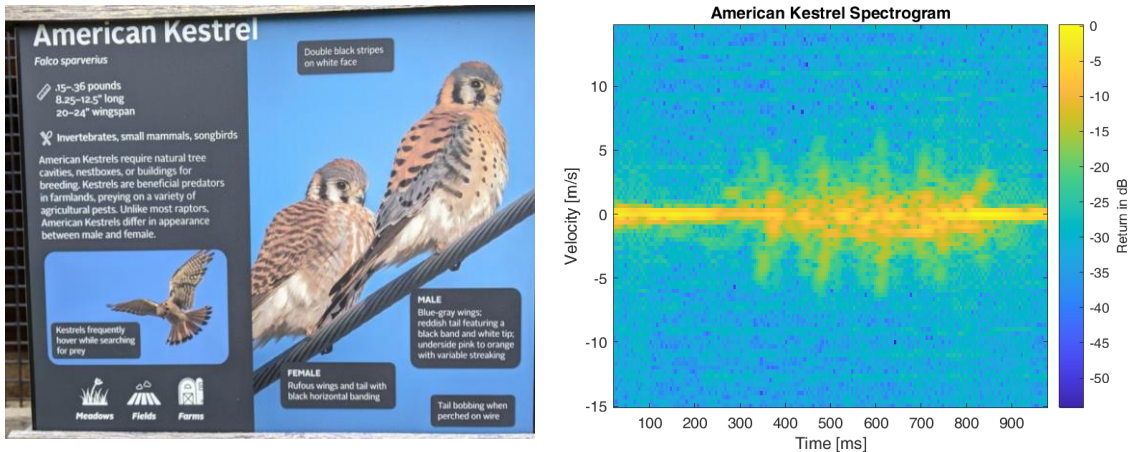


Figure 58: American kestrel and its associated spectrogram.

Figure 58 is the spectrogram of an American kestrel. Like the broad-winged hawk, the total Doppler bandwidth is quite small, but the flapping periodicity is higher than the big birds.

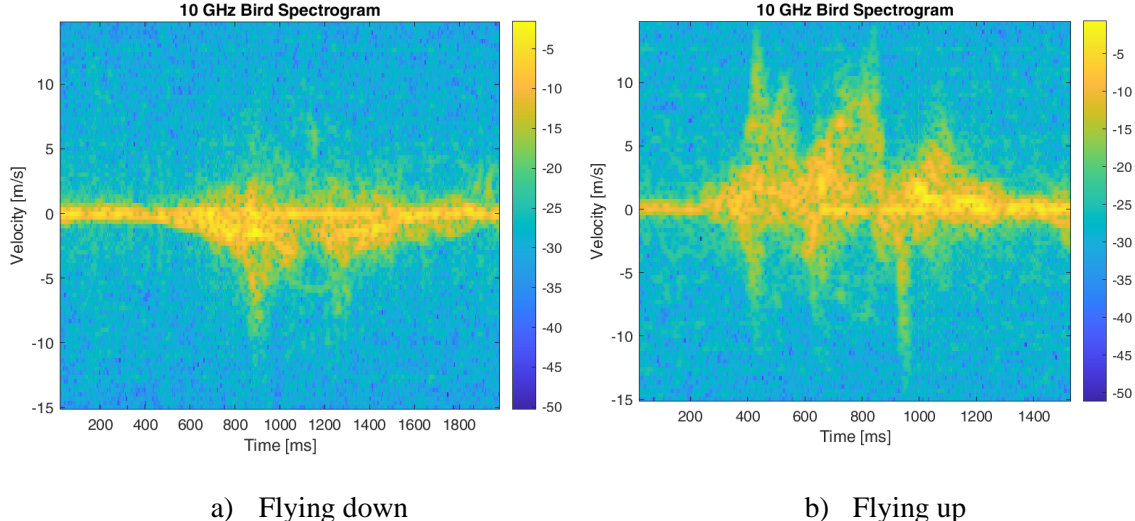


Figure 59: Bald eagle spectrograms flying lower vs. flying higher.

Figure 59 shows the comparison between a bald eagle flying down vs. flying up. The micro-Doppler bandwidth is larger when flying up, which makes sense since the wings need to flap harder to generate more thrust (Similar to the quadcopter).

Through bird data collection, the biggest challenge was getting the birds to fly. On hot days, the birds did not want to cooperate. This resulted in large recordings (5-10 minutes) for only a couple of recorded flights.

Another challenge was that one of the low noise amplifiers would heat up within a couple of minutes and render the system useless. If this happened before or during a bird flight, that flight was unusable.

4.5 – FMCW Micro-Doppler mmWave Studio Results

Using the 77-GHz FMCW, a collection of UAV evaluations was performed. Bird data were also collected, but for a variety of reasons, no significant data was obtained. This will be discussed further in the experimental limitations section.

mmWave Studio's post-processing window can analyze micro-Doppler, given an expected down-range. This can be provided by the Detection & Angle Estimation Results plot. After inputting the expected range, a spectrogram is generated. Since the velocity for the UAV blade rotations is much higher than the maximum pulse repetition frequency, a significant amount of aliasing occurs. For this reason, the micro-Doppler pattern does not accurately represent the true signature of the target like the CW radar does. The tradeoff is the ranging capabilities provided with this system. If used in tandem with the CW radar, this low-powered SDR can provide initial detection while the 10-GHz radar more accurately classifies the flying target.

Within mmWave Studio's post-processing feature, a spectrogram designed for micro-Doppler is possible, although it is incomplete.

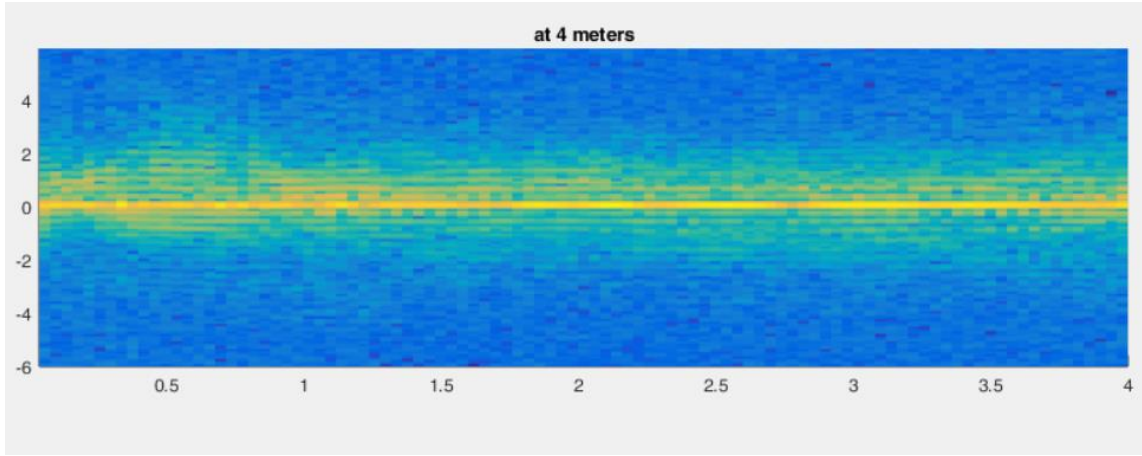


Figure 60: FMCW micro-Doppler within mmWave Studio.

In Figure 60, the micro-Doppler of the Akaso UAV is presented. It is greatly aliased compared to the 10-GHz CW radar. The *y*-axis denotes the velocity, and the *x*-axis denotes the time. Strong peaks are not present in this spectrogram.

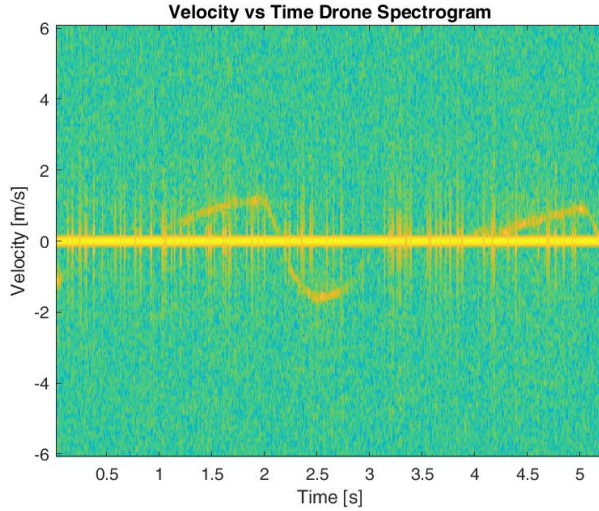


Figure 61: Outdoor UAV flight spectrogram.

Figure 61 shows a spectrogram of the Akaso drone flying outdoors but the micro-Doppler is not present. The main Doppler induced by the body of the UAV can be seen. One of the

reasons may be the low power output of the SDR. In Figure 62, the UAV is brought closer to the radar system. Although very faint, the micro-Doppler can be seen with hints of the blade tips around 8 m/s. Of course, this value is much lower than the true velocity.

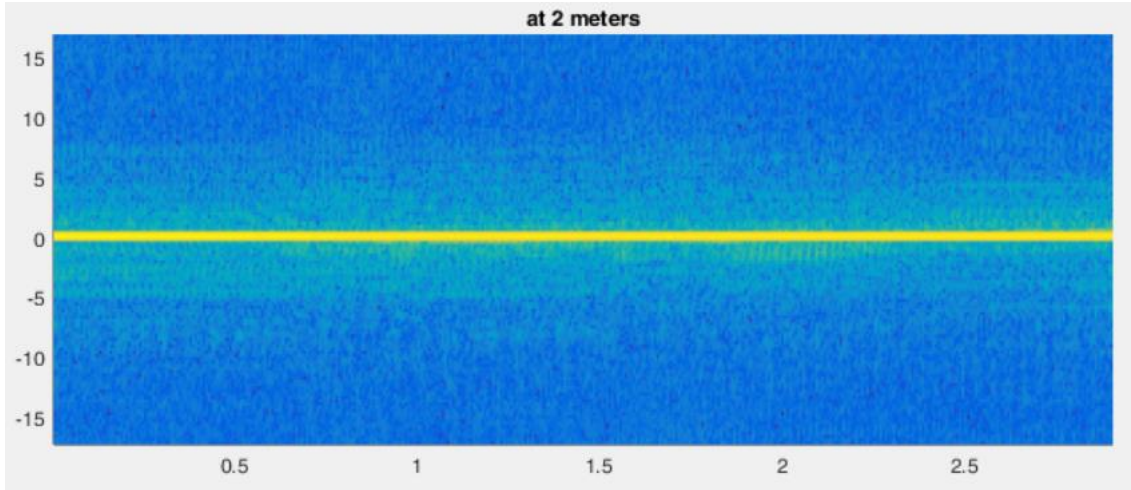


Figure 62: UAV micro-Doppler at 2 meters away.

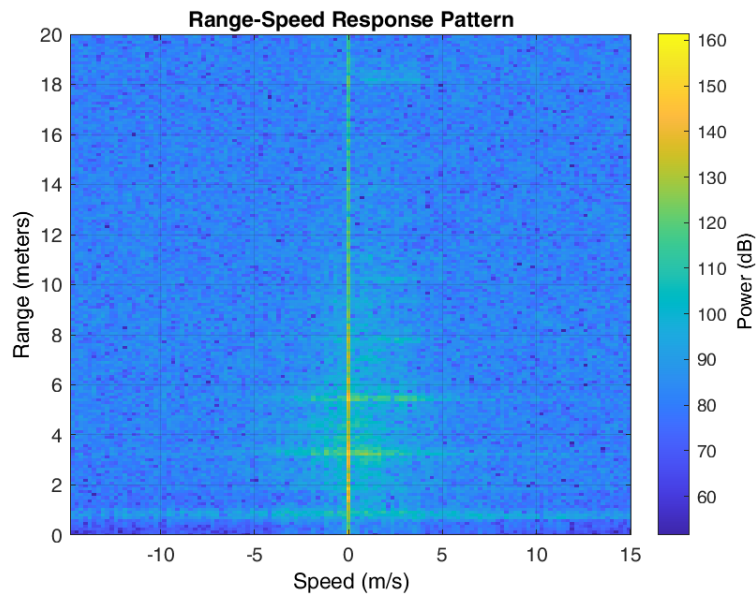


Figure 63: Range-speed response of an indoor UAV flight.

In Figure 63, the micro-Doppler in the plot of a range-speed response appears as a horizontal line that spreads across the entire axis. This is present around 1 meter away and the additional echoes are due to the indoor setup.

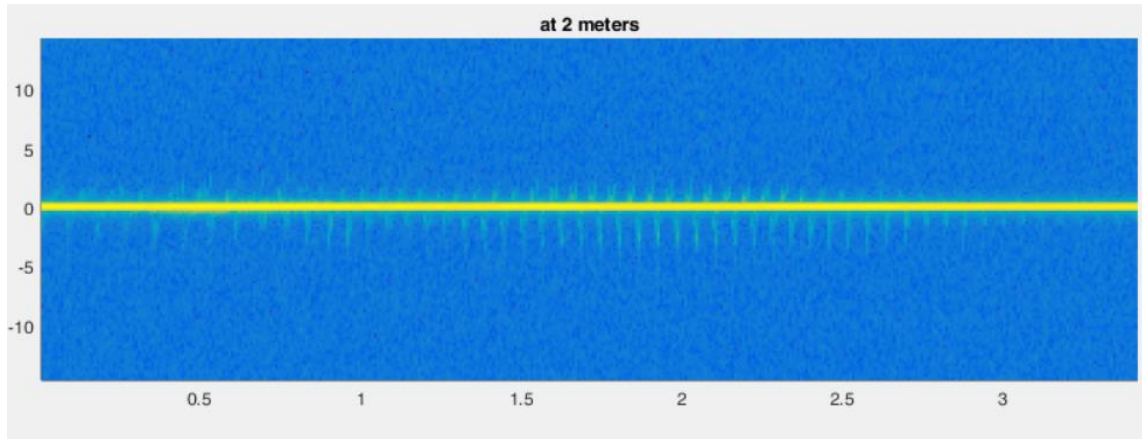


Figure 64: Metabird micro-Doppler through mmWave Studio.

In Figure 64, the micro-Doppler pattern for the Metabird is presented. Like Figure 62, the micro-Doppler is present although the velocity values are aliased.

4.6 Experimental Limitations

For the mmWave device's experiments, many limitations came in the form of the overall capabilities of the radar for performing the task of drone detection vs. automotive applications. Since this device was geared toward automotive applications, many of the characteristics of a vehicle differ from a flying target. The RCS of automotive targets is significantly higher, with a variety of different applications. Like using antennas with a wide frequency band, not all the applications will be suitable for the device. In terms of UAV detection, the SDR is capable, but not proficient.

When detecting bird micro-Doppler with the mmWave device, the enclosure provided surrounding clutter that made it difficult to detect the bird. The RCS of the main target was much lower than the objects around it. Since the birds were not detectable, neither was the accompanying micro-Doppler signature. Another limitation of the experiments regards the recording duration of the SDR. Due to the high sampling rate, large files were generated so recording times were restricted. This became troublesome when the birds did not want to fly when provoked.

Collecting bird data was a struggle due to their lack of willingness to fly. Since the bird enclosure was relatively small, it does not accurately depict a bird flying in free space.

Both the 10-GHz radar and the 77-GHz radar faced challenges when recording bird data. As mentioned previously, the 10-GHz CW radar could not operate for longer than two minutes, as a low-noise amplifier would overheat. For the 77-GHz system, the bird had to be monitored closely, and recording had to begin manually which made timing bird flights difficult. A solution was attempted to make the recordings longer, but file sizes became dramatically large. In addition, the visual accompaniment of PSI Studio occupied even more disk space. Another limitation is that most of the bird flights were perpendicular to the radar to highlight the flapping.

For experimental drone detection limitations, the flight behaviors of the drone were quite simple. For outdoor flights, the wind would play a large role in keeping the UAV within the LOS of the radar. In addition, the 77-GHz system faced great difficulty in detecting the targets, even within five meters away. For the UAVs themselves, the battery lives were quite short, resulting in roughly five minutes per charge.

Chapter 5 – Classification

For classification, the main features of interest are the total Doppler bandwidth and the micro-Doppler periodicity. With drones, the micro-Doppler bandwidth is much larger than the birds due to the high RPM of the spinning blades. In terms of periodicity, the drones have a constant micro-Doppler pattern since it is necessary to stay in flight. However, birds are not constantly flapping their wings.

5.1 – Spectrogram Generation

To begin classification, a large dataset was essential in providing confident results. To achieve this, many flights of each drone and bird were recorded. For UAVs, flights were snipped into equal segments. Only the spectrograms that contained the micro-Doppler signatures were kept. Initially, this work was done by reviewing PSI Studio footage and writing down the motion and duration of each segment as shown in Figure 65. This proved to be quite tedious.

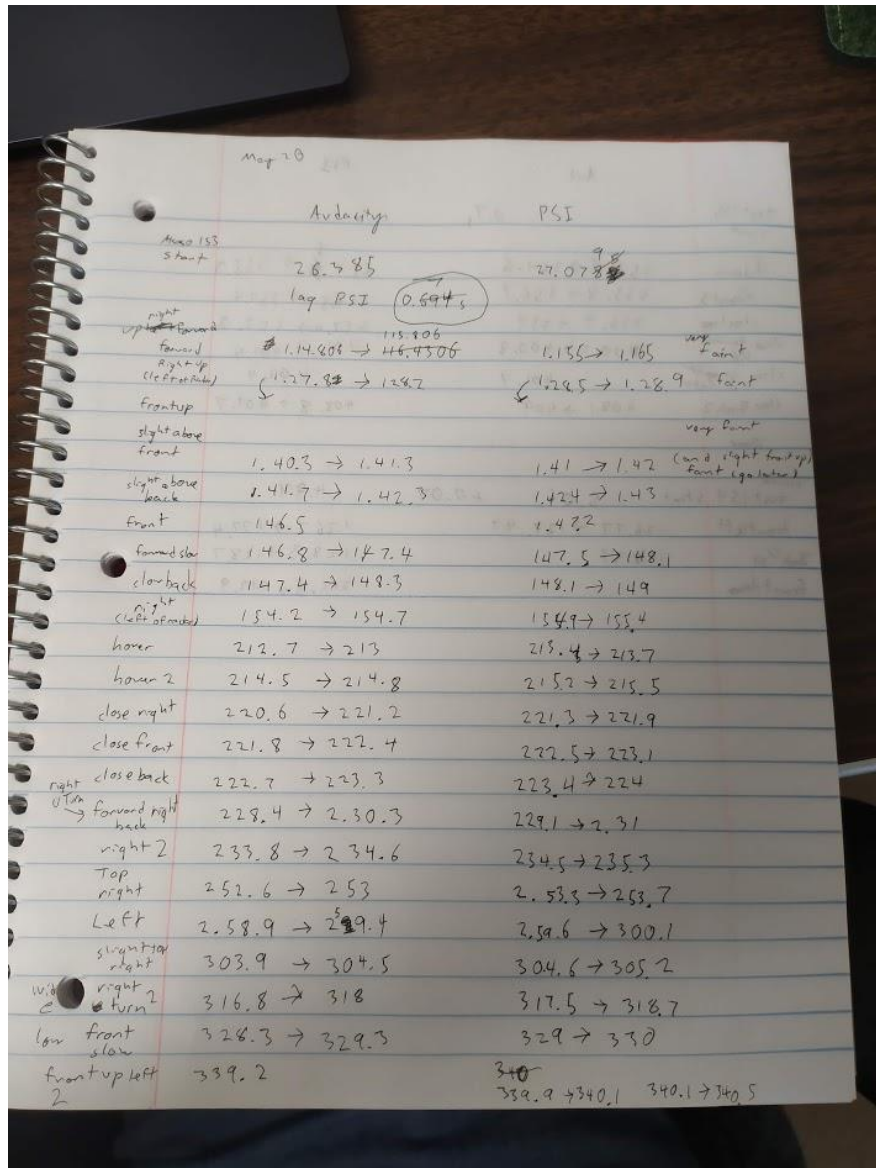


Figure 65: Early data sorting inefficiencies.

To expedite this ordeal, a shortcut was found within Audacity that could snip the overall .wav flight into smaller segments of the same length, as depicted in Figure 66.

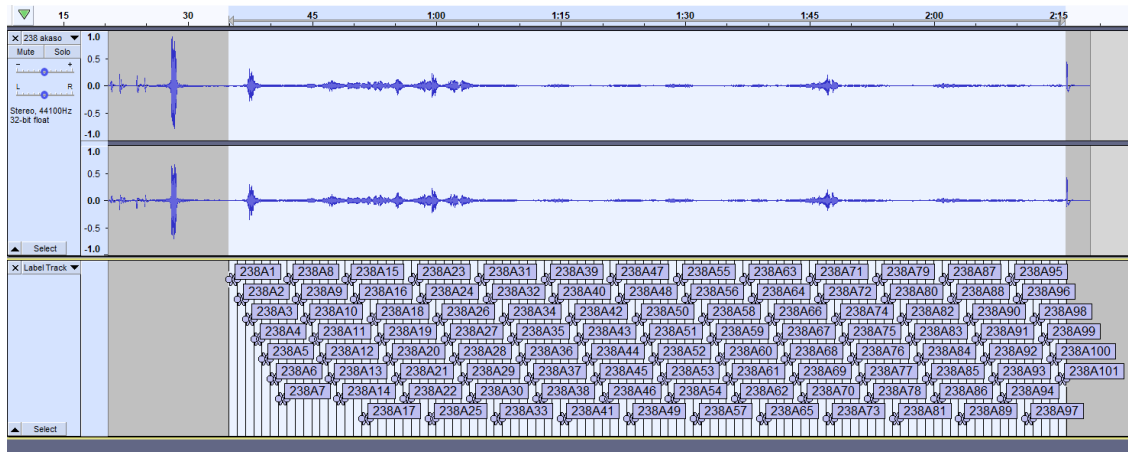
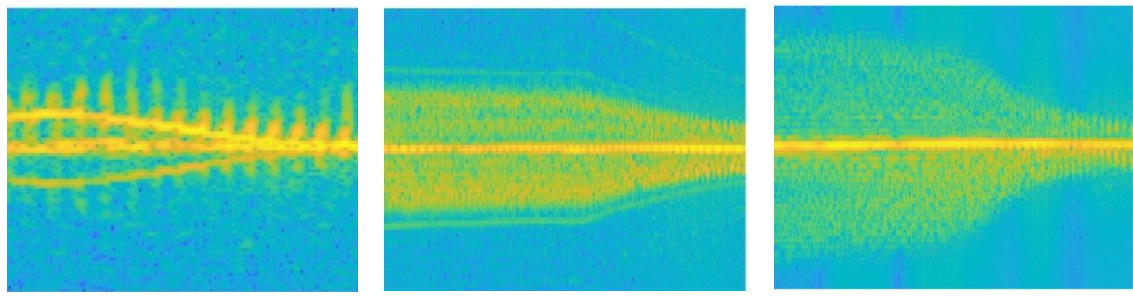


Figure 66: Expedited Audacity recording segment snipping.

The snipping process was expedited through an Audacity shortcut which allowed the overall .wav clip to be broken up into smaller, even segments.

Lastly, a MATLAB script was used to read every .wav file within a folder and generate spectrograms. The titles and axis labels are removed for each spectrogram and saved as .png files and stored within the database. The five classes of each target with removed labels are shown in Figures 67 and 68.



a) Metabird (Small) b) Akaso (Medium) c) BlackHawk (Big)

Figure 67: UAV spectrograms with removed axes and labels.

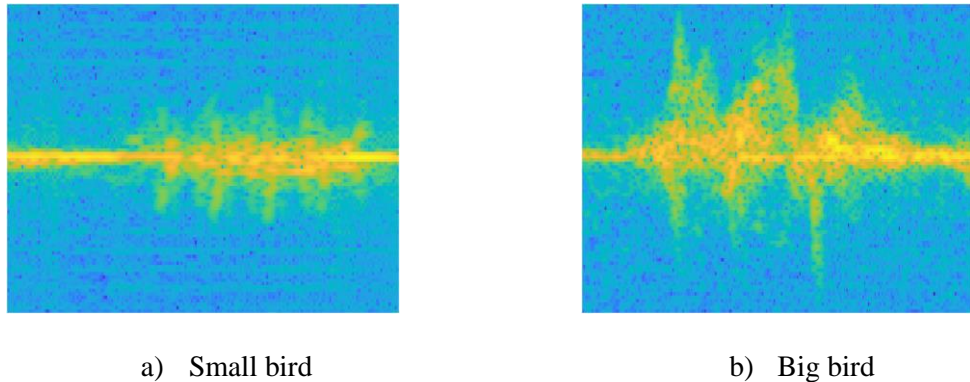


Figure 68: Bird spectrograms with removed axes and labels.

Before the images are classified within the TensorFlow environment, each image is set to 128×128 with a batch size of 32 and converted to greyscale.

5.2 – Support Vector Machine

For classification efforts, Support Vector Machine (SVM) was utilized. The SVM algorithm produces relatively high accuracy with low computational power. SVM is typically used in binary classification problems by separating two classes with an optimal hyperplane or decision boundary. This means maximizing the distance between data points from separate classes. By maximizing the distance between data points, images can be classified with higher confidence.

For classification efforts, the main features of concern are the micro-Doppler bandwidth and the micro-Doppler periodicity. The micro-Doppler bandwidth describes the maximum velocity achieved of the micro-motions while the periodicity gives insight into how often the motion occurs.

5.3 – Drone Classification

The first classification effort was conducted between distinguishing the three types of UAVs: small (Metabird), medium (Akaso), and big (BlackHawk). The dataset was split into 80% for training and 20% for testing. For testing, 86 UAV images were used. 10-Folds cross-validation was utilized to test the performance of multiple classifiers. Among eight candidates, the top three include logistic regression, SVM, and Random Forest. Overall, each class was distinguished with high confidence above 90%. In Figure 69, confusion matrices display the results of the classifiers. Out of the three, the SVM classifier performed the best.

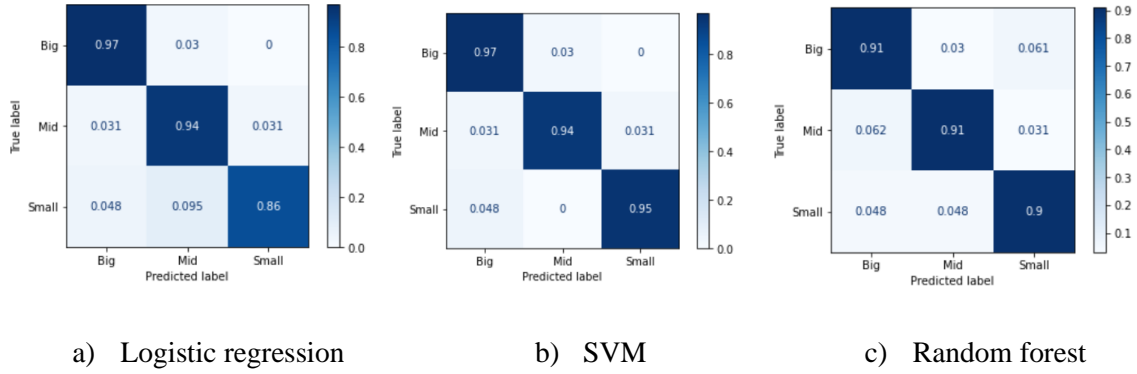


Figure 69: Confusion matrix results of classifier comparison for drone distinguishing.

The next classification test that was conducted involved only the Akaso UAV. In this study, the potential of distinguishing vertical motion states is explored. In Figure 70, spectrograms of rising, hovering, and falling micro-Doppler signatures are presented. It is important to note that these spectrograms are signifying the rotor behaviors of the drones and not the actual state of the UAV.

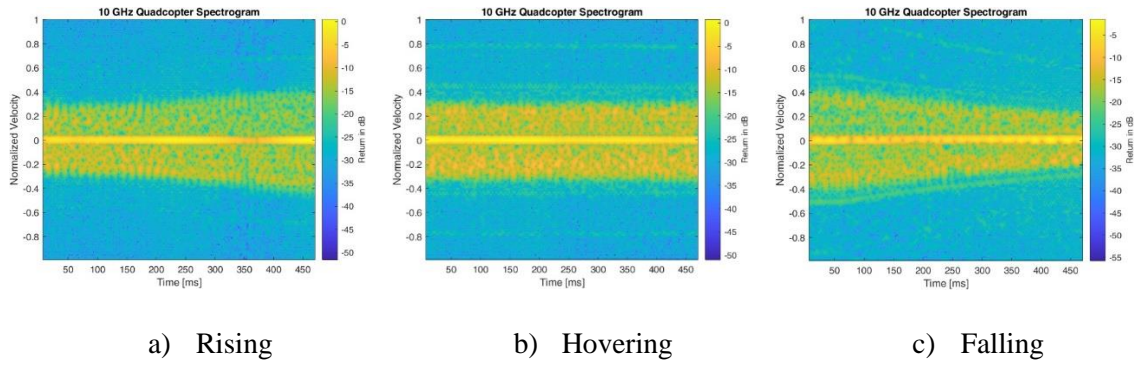


Figure 70: UAV rotor acceleration spectrograms.

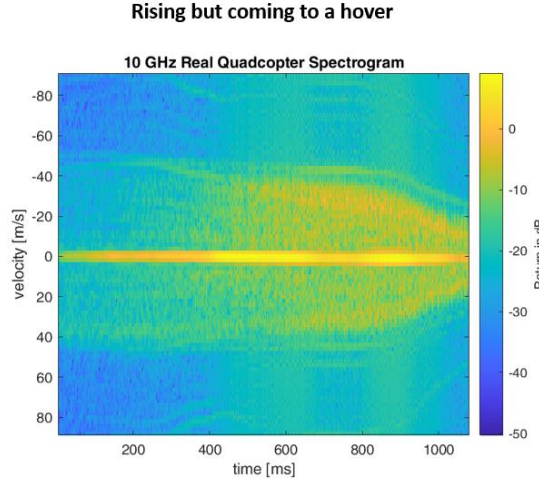


Figure 71: Deceptive spectrogram shows a UAV rising but coming to a hover with a falling shape.

In Figure 71, motion states are shown that show similar patterns to the spectrograms earlier but perform different UAV motions than what is suggested by the micro-Doppler signature. For example, although there is a decrease in the overall micro-Doppler bandwidth over time, the UAV is rising but slowing down and begins to hover.

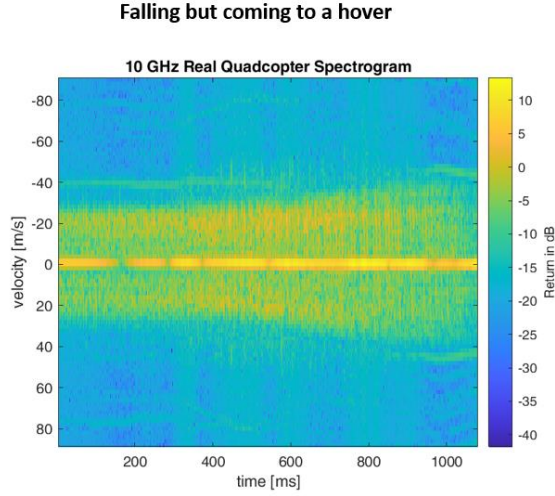


Figure 72: Spectrogram shows a UAV falling and coming to a hover but with a rising shape.

In Figure 72, the micro-Doppler pattern shows an acceleration in rotor speed, hinting at a rising body state, but the UAV is initially falling and starts to come to a hover over time.

The dataset of motion states consists of Akaso 218 micro-Doppler images. This was split into 80% for training and 20% for testing. A sequential model is used with two 2D convolutional layers with the ‘relu’ activation function. After each 2D convolutional layer, a max-pooling 2D layer is utilized followed by a 20% dropout layer. Finally, the shape is flattened, and two dense layers are used. The total parameters within this model are 2,100,435. The model summary is shown in Figure 73.

```

Model: "sequential"
-----  

Layer (type)          Output Shape       Param #
-----  

rescaling (Rescaling) (None, 128, 128, 3)    0  

conv2d (Conv2D)        (None, 128, 128, 16)   448  

max_pooling2d (MaxPooling2D) (None, 64, 64, 16) 0  

dropout (Dropout)      (None, 64, 64, 16)    0  

conv2d_1 (Conv2D)      (None, 64, 64, 16)    2320  

max_pooling2d_1 (MaxPooling2D) (None, 32, 32, 16) 0  

dropout_1 (Dropout)    (None, 32, 32, 16)    0  

flatten (Flatten)      (None, 16384)       0  

dense (Dense)          (None, 128)         2097280  

dense_1 (Dense)        (None, 3)           387  

-----  

Total params: 2,100,435  

Trainable params: 2,100,435  

Non-trainable params: 0
-----
```

Figure 73: Drone motion state model summary.

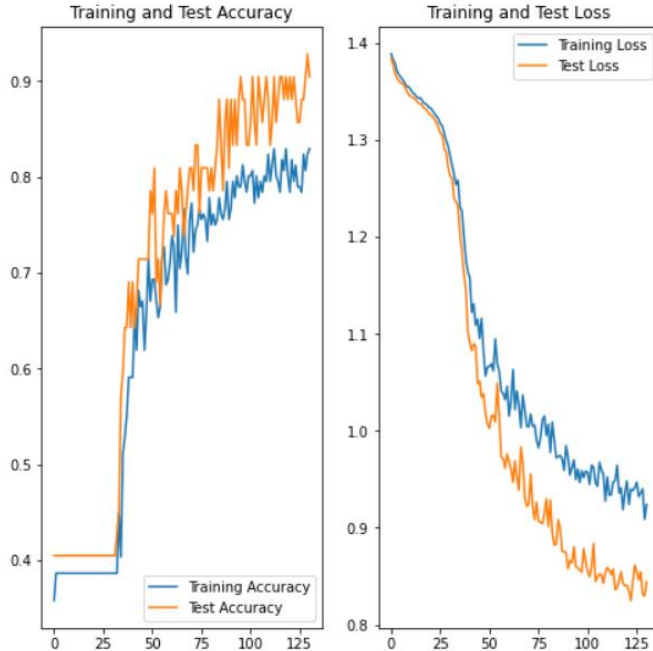


Figure 74: Drone motion state classification accuracy and loss.

In Figure 74, the results of the classification using SVM are shown in distinguishing the different acceleration patterns of the UAV. At 130 epochs, 92.86% confidence is obtained. The

training accuracy is lower than the test accuracy due to the use of a dropout layer in training. The test loss submerges 0.9 after roughly 80 epochs.

5.4 – Binary Classification

Next, bird micro-Doppler images are included in classification efforts. Initially, a binary classification task for distinguishing drones and birds is conducted. The `sklearn.svm` toolkit was utilized with the `linearSVC` classifier with a max iteration of 1000. The linear SVC uses the l2 penalty and a squared-hinge loss function with 0.0001 tolerance.

With a 2/3 training and 1/3 testing split, 152 drone images and 86 bird images were used for testing. The confusion matrix in Figure 75 shows high accuracy in classifying between drones and birds with a 96% accuracy. The precision for drones is 98% and for birds is 92%.

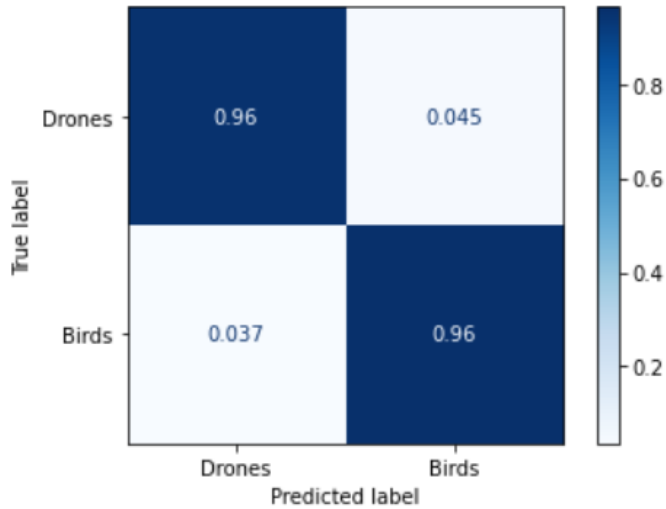


Figure 75: Drones vs. birds confusion matrix.

5.5 – 5-Class Classification

For multi-class classification, the SVM classifier utilizes a one-versus-rest scheme. This strategy splits the five-class dataset into multiple binary classification problems. In this classification problem, the three separate UAVs are considered in addition to the big and small bird categories. The big birds consist of the bald and golden eagles while the small birds pertain to the broad-winged hawk and American kestrel. Figure 76 shows the confusion matrix for the 5 classes.

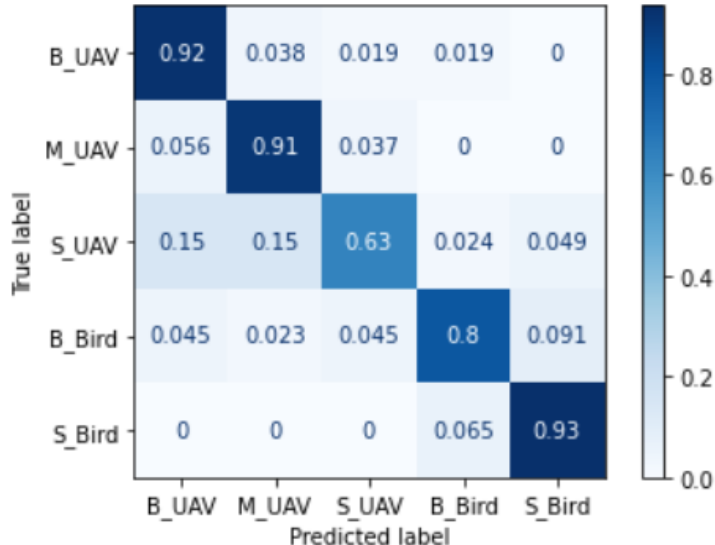


Figure 76: 5-Class confusion matrix.

The quadcopters and small birds are classified with strong confidence while the Metabird and the big birds have a harder time. For the big birds, the confusion is across the board but is mostly mistaken for a small bird. The inaccuracy within the small UAV class, Metabird, may be due to a smaller number of images available for training and testing. Most of the mispredictions of the Metabird are the other drones.

5.6 – Classification Limitations

Some of the limitations include the amount of data available for testing. More flights should be collected to improve confidence, especially for the 5-class classification. With more variety in micro-Doppler signatures, the accuracy of distinction could be increased significantly.

Chapter 6 – Conclusions

This thesis consists of data collected by a custom-designed radar system, utilized in different scenarios with a variety of targets. A dataset was created based on the micro-Doppler images obtained and classification results were achieved with high confidence. Different characteristics of target detection were explored, including the landscape and the behavior of the target.

Future work regarding this field would include methods for automating a method for detecting targets with the low-powered SDR, then notifying and turning on the 10-GHz radar to collect the micro-Doppler signature. This would allow for more efficient automatic target recognition.

Another avenue for future work would involve the distinction in UAV motion as the target rolls and pitches in different directions. Due to the cluttered motions in the varying velocities, it would be of interest to design an algorithm for separating these rotor velocities and characterizing the overall target motion. Detecting micro-Doppler signatures in urban or cluttered areas would also be beneficial.

With micro-Doppler images, classification efforts regarding UAV motions and target recognition can be confidently characterized.

References

- [1] J. O’Malley, “The no drone zone,” *Engineering & Technology*, vol. 14, no. 2, pp. 34–38, March 2019, doi: 10.1049/et.2019.0201.
- [2] J. Markow and A. Balleri, “Examination of drone micro-Doppler and JEM/HERM signatures,” in *Proc. 2020 IEEE Radar Conference (RadarConf20)*, On-line, September 2020, doi: 10.1109/RadarConf2043947.2020.9266342.
- [3] R. I. A. Harmanny, J. J. M. de Wit, and G. P. Cobic, “Radar micro-Doppler feature extraction using the spectrogram and the cepstrogram,” in *Proc. 2014 11th European Radar Conference*, Rome, Italy, October 2014, doi: 10.1109/EuRAD.2014.6991233.
- [4] P. Molchanov, K. Egiazarian, J. Astola, R. I. A. Harmanny, and J. J. M. de Wit, “Classification of small UAVs and birds by micro-Doppler signatures,” in *Proc. 2013 European Radar Conference*, Nuremberg, Germany, October 2013, pp. 172–175.
- [5] J. Gérard, J. Tomaszik, C. Morisseau, A. Rimmel and G. Vieillard, “Micro-Doppler signal representation for drone classification by deep learning,” in *Proc. 2020 28th European Signal Processing Conference (EUSIPCO)*, On-line, January 2021, pp. 1561–1565.
- [6] V. C. Chen, F. Li, S.-S. Ho, and H. Wechsler, “Micro-Doppler effect in radar: phenomenon, model, and simulation study,” *IEEE Transactions on Aerospace and Electronic Systems*, vol. 42, no. 1, pp. 2–21, January 2006, doi: 10.1109/TAES.2006.1603402.
- [7] Rao, Sandeep, “Introduction to mmwave Sensing: FMCW Radars,” [Online]. Available: https://training.ti.com/sites/default/files/docs/mmwaveSensing-FMCW-offlineviewing_4.pdf.
- [8] B. Taha and A. Shoufan, "Machine Learning-Based Drone Detection and Classification: State-of-the-Art in Research," in *IEEE Access*, vol. 7, pp. 138669-138682, 2019, doi: 10.1109/ACCESS.2019.2942944.
- [9] Texas Instruments (2017), “AWR1642 Evaluation Module (AWR1642BOOST) Single-Chip mmWave Sensing Solution,” [Online]. Available: <https://www.ti.com/lit/ug/swru508c/swru508c.pdf>.
- [10] Texas Instruments (2017), “mmWave Studio User Guide,” [Online]. Available: https://software-dl.ti.com/ra-processors/esd/MMWAVE-STUDIO-2G/latest/index_FDS.html.